

POLITECNICO DI TORINO

Master Degree in Electronic Engineering



Master Degree Thesis

**Cross-correlation measurements for the
analysis of noise sources in a resonant
laser propagating into an atomic vapor**

Supervisors

Giovanni Antonio Costanzo

Michele Gozzelino

Claudio Eligio Calosso

Candidate

Modestino Carbone

s310477

April 2025

Table of Contents

List of Tables	IV
List of Figures	V
Acronyms	X
1 Introduction	1
1.1 Rubidium Vapor-cell clocks	3
1.2 POP Clock	5
1.3 Error Signal Generation	9
2 Noise Contributions	12
2.1 Relative Intensity Noise of the Laser	13
2.2 Shot Noise	14
2.3 Brownian Noise	14
2.4 PM-AM Noise	17
3 Cross-correlation	18
3.1 Basics	19
3.2 Statistical Tools	21
3.3 Cross-spectrum Estimators	24
3.3.1 Artifacts in the Cross-correlation Spectrum	26
3.4 Experimental Test Bench for Measuring the Intensity Noise Contributions	28
4 Instruments Characterization	31
4.1 DAQ	31
4.2 DFB (Distributed Feedback) Laser Diode	38
4.3 Photodiode	39
4.3.1 Single Photodiode	39
4.3.2 Balanced Photodiode	41

5	Measurement Technique for Relative Intensity Noise	45
5.1	Laser Shot Noise Measurement with Balanced Acquisition	46
5.2	Laser Technical Noise	49
6	Measurement Technique for Atomic noise	52
6.1	Introduction on Atomic Absorption	53
6.1.1	Doppler Broadening	54
6.2	Calibration: Rb cell saturated absorption spectroscopy	56
6.3	Absorption Profile of the Rubidium Cell with Buffer Gas	60
6.4	AM Noise Atom Interaction	62
7	Conclusions and Perspectives	67
A	Python Spectrum Functions (Spectra_lib.py)	69
A.1	PSD	69
A.1.1	Bartlett's Method	70
A.1.2	Welch's Method	70
A.1.3	Python Code	72
A.2	CSD	74
A.2.1	Python Code	75
A.3	Advanced Averaging Methods	76
A.3.1	Python Code with Maximum Averages	77
A.3.2	Python Code with Minimum-Maximum Averages	79
B	Example of Cross-correlation Estimation	82
C	Allan Variance	85
D	Fitting Models	87
	Bibliography	90

List of Tables

3.1	Table of values of the variances referred to the random process X and Y	23
4.1	DAQM909A module features	32
4.2	Default condition of measures	35
4.3	Eagleyard EYP-DFB Laser characteristics	38
4.4	Thorlabs PDA36A2 Photodiode features	40
4.5	Thorlabs PDB250A Photodiode features.	42
6.1	Strength factors and frequency offset for ^{87}Rb , taken from [36] . . .	58
6.2	Fitting results of the triple Gaussian fit	59

List of Figures

1.1	Example of triangulation in a 2-D world. Satellites S1, S2 , S3 are necessary to estimate the position of the point P.	3
1.2	Airbus RAFS clock, taken from [8]	4
1.3	NIST chip scale atomic clock developed in 2011, taken from [10]	5
1.4	Energy levels of ^{87}Rb	6
1.5	Ramsey scheme	6
1.6	Example of a Ramsey-fringe patterns dependent on the microwave detuning, calculation follows the theory developed in [13]. This plot is centered at the natural frequency of the rubidium shifted due to the buffer gas.	7
1.7	POP schematic, taken from [14]. Dashed frames include optics (OP), physics (PP) and electronics (EP) subsystem	8
1.8	Simplification of a complete vapor-cell clock schematic. PD1 is the photodiode that detects the atomic signal, which is used to detect the clock transition, image was taken from [18]	9
1.9	absorption function $I(\nu)$	10
1.10	error function of ΔI , $\Delta I = I(\nu_s + \delta\nu) - I(\nu_s - \delta\nu)$	10
1.11	Clock stability of a POP clock (black line), taken from [20]	11
2.1	lateral view of the cell illuminated by a laser beam	12
2.2	Simulation of three pollen particles suspended in water that covers a Brownian motion; initial position $(x,y) = (0,0)$; initial speed $(v_x,v_y)=(0,0)$	14
2.3	Laser intensity distribution for $w = 0.34$ mm	15
2.4	Phase noise example in a generic rubidium absorption profile, y-axis represents relative absorption $L = I(\nu_L)/I_0$	17
3.1	Basic cross-spectrum measurement	19
3.2	3D visualization of the selection of a specific frequency in the sequence of $\langle S_{yx} \rangle_i$	21

3.3	Average and standard deviation at the increasing of "m", averaging factor	23
3.4	Single spectrum contribution for a(t), b(t), c(t), d(t) of the equation 3.20	26
3.5	Cross-correlation between x and y compared with x and the version of y which contains an anticorrelated contribution \tilde{y} (eq. 3.21) . . .	27
3.6	Noise contribution in a simple acquisition absorption setup. In the figure: arrow represents a laser beam, PD1 is a photodiode, ADC is a analog to digital converter.	28
3.7	measurement setup for laser technical noise. In the figure: arrow represents a laser beam, PD1 ans PD2 are photodiodes, ADCs are the channels of th analog to digital converter.	29
3.8	measurement setup for rubidium atomic noise and technical laser noise. In the figure: arrow represents a laser beam, PD1 ans PD2 are photodiodes, ADCs are the channels of th analog to digital converter.	29
3.9	measurement setup for rubidium atomic noise. In the figure: arrow represents a laser beam, PD1-PD4 are 4 photodiodes, ADCs are the channels of th analog to digital converter.	30
4.1	Keysight DAQ970A instrument, photo taken from [32]	32
4.2	Keysight DAQ970A input gain bandwidth	33
4.3	Aliasing effect when the sampling frequency is 20 kHz	34
4.4	Aliasing effect when the sampling frequency is 50 kHz	34
4.5	50 Ω termination measure (blue line), noise mean was performed between $[10^3 - 10^4]$ Hz (orange line)	35
4.6	50 Ω Noise vs Theoretical quantization noise. The theoretical value of the quantization noise in red dashed line (-209.6 dB V^2/Hz) compared with the input noise in orange line (-152 dB V^2/Hz) . . .	37
4.7	EYP-DFB Eagleyard Photonics Distributed Feedback Laser	38
4.8	Thorlabs PDA36A2 Si Switchable Gain Detector: (a) Physical package, (b) Responsiviy, taken from [33]	39
4.9	Dark noise of a single photodiode with variable gain 0 dB (blue curve), 10 dB (green curve), 30 dB (red curve).	41
4.10	Thorlabs PDB250A Si Switchable Gain Balanced Detector: (a) Physical package , (b) Responsiviy, taken from [34].	42
4.11	Measured differential Gain steps vs the RIN of the RF channel following the definition of 4.14 with no input power. The RIN is performed assuming a monitor power of 100 μW	44
4.12	RIN of the dark noise with varying normalization power levels (100 μW , 20 μW , 2 μW)	44

5.1	Simplified double photodetector setup. In the scheme are presented a polarizing beam splitter, a mirror and a balanced Thorlabs photodiode (red box), see section 4.3.2.	46
5.2	Double photodetector setup results, data are collected for a laser power of 20 uW. In the image: theoretical shot noise (orange curve), dark noise when laser power is not present (green curve) and the RIN_N of the differential measure.	47
5.3	Double photodetector setup results, data are collected for a laser power of 4.6 uW. In the image: theoretical shot noise (orange curve), dark noise when laser power is not present (green curve) and the RIN_N of the differential measure.	48
5.4	Simplified RIN measurement optical setup (PD1 and PD2 are two photodiodes while PBS a polarizing beam splitter).	49
5.5	Technical noise setup results fixing the input power detected by photodiodes at 20 μW	50
5.6	Technical noise setup results fixing the input power detected by photodiodes at 160 μW	50
5.7	Technical noise setup results fixing the input power detected by photodiodes at 470 μW	51
6.1	Figurative description of the extinction law 6.2 with a laser (red arrow) crossing an atomic medium (blue dots).	53
6.2	Δz vertical section of a cell containing an atomic medium (blue dots).	54
6.3	Block diagram representation of measurement circuit used for absorption profile	56
6.4	Rubidium atoms (blue dots) and their velocity (green vectors), magenta vectors highlights the condition $v_z = 0$	57
6.5	^{87}Rb absorption spectrum red dots highlights the reference calibration "dips": cross-over CO13, CO23 and the energy level $F'=3$	57
6.6	^{87}Rb energy levels, cross-over levels are represented with red dashed lines.	58
6.7	^{87}Rb absorption spectrum with triple gaussian fit; dashed lines highlights: the complete absorption curve of the formula 6.10 (green curve), $F'=1$ gaussian (magenta), $F'=2$ gaussian (cyan), $F'=3$ gaussian (yellow).	59
6.8	Calibration figure: reference frequency based on the pure rubidium absorption profile (Blue curve); the DC absorption profile of the cell diluted in buffer gas (Green curve).	60

6.9	Final configuration: (a) Optical schematic of the acquisition setup, showing balanced photodiodes (highlighted in red), three beam splitters (BS1 - BS3) and a rubidium cell (gray box). (b) Physical implementation of the system.	62
6.10	Figure shows the cross-correlation plot of the two differential photodiodes RF channels in correspondence of the maximum absorption coefficient, (Tuning the laser in the center of Lorentzian). The blue spectrum in the picture, the RF1 channel is compared with the two estimator or cross correlation $\Re\{S_A\}$ (green and red line) and $ S_A $ (dashed orange line).	63
6.11	Colored points: MIN, P2, P3, P4, P5; they represent the operational points at which the intensity noise spectrum was measured.	64
6.12	A zoomed portion of the cross-spectrum in the $[10^3 - 10^5]$ Hz spectrum range comparing the cross-spectrum measured in the maximum absorption point (blue curve) with the value obtained obscuring photodiodes (magenta line). The values of the cross-spectrum when the laser is tuned at 2Γ (black line).	65
6.13	The image displays the magnitude of the measured atomic noise at a fixed Fourier frequency of 2 kHz. The x-axis represents the laser frequency, vertical bars are instead a visual representation of the uncertainty of the measurement.	66
A.1	Two possibility of window framing are showed bigger windows used for lower Fourier bins, smaller one for higher Fourier bins	77

Acronyms

AVAR

Allan variance

ADEV

Allan deviation

CPT

Coherent Population Trapping

CSAC

Chip Scale Atomic Clock

CSD

Cross-Spectral Density

DUT

Device Under Test

FFT

Fast Fourier Transform

GNSS

Global Navigation Satellite System

PBS

Polarizing Beam Splitter

POP

Pulsed Optical Pumping clock

PSD

Power Spectral Density

RAFS

Rubidium Atomic Frequency Standard

SCPI

Standard Commands for Programmable Instruments

Acknowledgements

A Nonna Angela
sempre presente
nonostante la distanza

Chapter 1

Introduction

Atomic clocks can be considered as the cornerstone of the development of GNSS (Global Navigation Satellite System), aerospace and telecommunication technologies. Without the usage of proper timekeeping devices location services would not be possible. The accuracy of location services relies on precise timekeeping, since GNSS satellites determine position by measuring the time it takes for signals to travel between the satellite and the receiver. Without highly stable clocks, errors in time measurement would translate into significant errors in positioning. The functionality of tracking satellite constellations, including GPS, GALILEO, and COMPASS, relies on the same technological innovation: rubidium vapor-cell clocks [1]. The rubidium vapor-cell is the beating heart of this kind of atomic clock, ensuring superior short-term frequency stability. Unlike quartz oscillators, which gradually lose accuracy due to drift, rubidium clocks utilize atomic transitions to sustain a highly stable reference frequency [2] [3].

Atomic clocks function by exploiting the natural oscillations of atoms as a highly stable frequency reference. In a rubidium vapor-cell clock, a laser tuned to a specific frequency interacts with rubidium atoms, exciting them to a higher energy state. The system then locks onto the precise frequency of this atomic transition, ensuring an exceptionally stable time reference. Any fluctuations in atomic behavior, such as movement within the vapor cell, can introduce noise and affect the clock's accuracy. Given the critical role of frequency stability in atomic clocks, understanding and mitigating noise sources is essential. In this context, precise characterization of atomic noise becomes a fundamental step in improving clock performance.

Cross-correlation techniques are used to separate intrinsic atomic noise from other noise sources, such as electronic or optical fluctuations. By comparing signals from multiple independent detection channels, it is possible to isolate the common atomic noise while suppressing uncorrelated background noise. This method enhances the accuracy of noise characterization and contributes to the overall stability of atomic clocks.

This thesis was conducted in collaboration with the National Institute of Metrological Research (INRIM). The institute hosts the Scientific Department of Time and Frequency, specialized in time references and the development of atomic clocks. INRIM is also the Italian authority responsible for distributing the UTC(IT), the legal time reference for Italy.

The subject of this thesis work is the definition of a method that allows the measurement of the atomic noise of a vapor cell. This noise contribution can be measured analyzing the intensity spectrum of the light passing through the atomic medium. The proposed set-up achieved this goal using a differential setup, where the measurement of cross-correlated channels is used to enhance the atomic noise signal. The definition of an effective methodology is based on the theoretical knowledge of the mathematical methods used and the physical phenomena involved. At a later stage, the actual measurement of the intensity noise will be approached and processed in order to obtain the desired result.

A brief list of the topics that will be covered:

- In *section 1.1* atomic clocks and rubidium vapor-cell clocks working principles are described, with a focus on the relation between absorption intensity noise and clock uncertainty.
- *Chapter 2* offers an overview to the different types of noise contributions that constitutes the total intensity noise that affects a vapor cell absorption measurement.
- *Chapter 3* is a mathematical description of the cross-correlation in his theoretical and statistical characteristics. As a natural consequence, the integration between this processing technique and the optical circuit is also investigated.
- In *Chapter 4* every electronic devices is thoroughly examined in order to list main characteristics of the instruments involved for the subsequent measures.
- In *Chapter 5* a preliminary set of measures are performed with the aim of estimating the laser technical noise and the shot noise of the system.
- In *Chapter 6* a final measurement setup and a custom method are implemented for the atomic noise detection.

1.1 Rubidium Vapor-cell clocks

Atomic clocks were designed and imagined since the beginning of the World War II, at that time, the USA still relied on quartz oscillators as its time standard. In 1939, the physicist Isidor Isaac Rabi proposed, at the National Bureau of Standards (NBS) [4], the introduction of a new timekeeping devices which relies on a new magnetic resonance technique. In 1944 Rabi was awarded with the Nobel Prize. One of the most significant consequences of his work was the redefinition of the second (still used today), based not on astronomical observations but on the natural frequency of cesium, approximately 9.1914 billion oscillations per second. This shift from using Earth's rotation to measure time to relying on the stable atomic properties of cesium marked a transformative moment in the history of timekeeping, laying the foundation for the precise atomic clocks that we rely on today. Among the various types of atomic clocks, rubidium vapor-cell clocks (also called an Rb oscillator) are a type of atomic clock that relies on the hyperfine transition of rubidium atoms. Unlike cesium atomic clocks, which use a beam of atoms in a vacuum, rubidium clocks operate using a small glass vapor cell containing rubidium gas mixed with an inert buffer gas. Due to its characteristics, it was initially developed as a laboratory instrument and soon after adopted for tactical military communications. In 1977, the USA GPS program was launched with both cesium and rubidium-based clocks. Nowadays rubidium vapor-cell clocks play a big role in the Global Navigation Satellite Systems (GNSS), the 31 active GPS satellites embed four rubidium-based atomic clocks updated daily [1] [5].

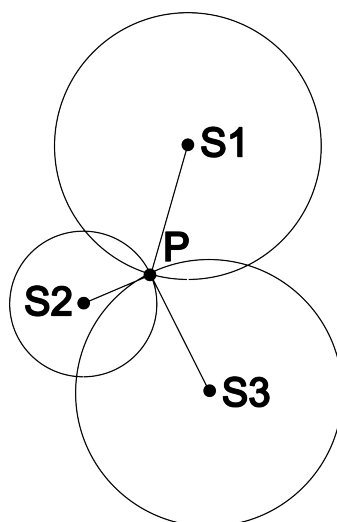


Figure 1.1: Example of triangulation in a 2-D world. Satellites S1, S2 , S3 are necessary to estimate the position of the point P.

GPS systems determine their location by measuring the time it takes for signals to travel from multiple satellites. Since radio waves move at the speed of light, even a nanosecond-level error in timekeeping could introduce significant positioning errors, potentially several meters in location accuracy. To determine a user's position, a GPS receiver relies on a technique called trilateration. In order to determine the position of a point in a n -dimensional space, $n+1$ measurements are needed. This concept in a 2-D space is called triangulation because only 3 detectors are needed to evaluate the position (fig.1.1). In a 3-D world at least 4 satellites are needed to determine position which can be expressed by the triple: latitude, longitude and altitude [6]. GNSS engineers evaluate the advantages of a frequency Standard using as primary thumb rule three distinct parameters: its size, weight and power requirements (SWaP). The correct trade-off between these characteristics makes the best design solution. The working principle of satellite atomic clocks is substantially unchanged overtime and it consists in a space-qualified OCXO (ovenized crystal oscillators) frequency-locked to an atomic hyperfine transition [7].

The Rb resonant frequency, 6.835 GHz, can be revealed by a photodiode but in order to trigger this transition engineers must create a compact space-compatible radiating source. Using an electrodeless Rb discharge lamp the correct nominal wavelength was naturally emitted by the rubidium plasma. The lifespan of an RF-discharge lamp is limited primarily due to the gradual depletion of rubidium atoms and the degradation of the glass enclosure caused by prolonged exposure to plasma emissions. If the rubidium quantity is too high, it can generate excessive noise. Conversely, if the amount of rubidium is too low, a significant percentage of atoms diffuse into the glass, causing the remaining rubidium concentration to be too low to produce sufficient plasma emission. The discharge lamp clock is a technology that needs maintenance of 20 years, it was the first light source introduced for this kind of devices.



Figure 1.2: Airbus RAFS clock, taken from [8]

Unlike RF-discharge lamps, lasers provide an ideal light source thanks to their

narrower bandwidth and higher efficiency. The introduction of laser sources changes the approach of timekeeping devices and introduces new laser clocks like the Coherent Population Trapping (CPT) clock or the pulsed optical pumping (POP) scheme. The introduction of the CPT technique unlocks a new category of chip-scale atomic clocks (CSAC) [9], smaller size, lower power consumption, and lower cost. CPT clocks presents two phase-coherent lasers interact with the atomic vapor-cell with a certain difference in frequency but equal intensities for the purpose of containing the light-shift effect. CSACs can reach a physical dimension of 20 cm^3 .

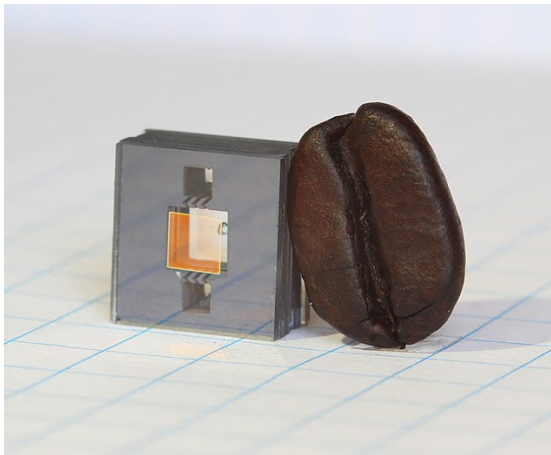


Figure 1.3: NIST chip scale atomic clock developed in 2011, taken from [10]

1.2 POP Clock

Starting from 2012, INRIM has developed and characterized a specific frequency standard working in a pulsed regime named rubidium vapor-cell called Pulsed Optically Pumped (POP) clock [2]. The working principle of this device is based on three time slotted phases: *preparation*, *interrogation*, and *detection*.

First the laser, passing through the Rb cell at a specific resonance frequency, pumps atom from the level $5^2S_{1/2}$ to the energy level $5^2P_{3/2}$ (see figure 1.4). This transition called D_2 makes atom going back, if power is enough, to the initial ground state. Due to hyper-fine structure atoms can populate the energy level $5^2S_{1/2}$ $F = 2$ but also the level $5^2S_{1/2}$ $F = 1$. After this step of *preparation*, if the pumping rate was sufficiently high, a population imbalance between the two ground states is achieved.

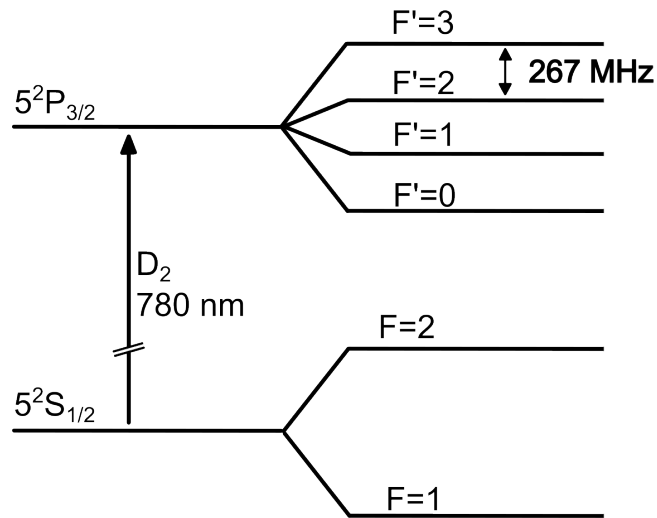


Figure 1.4: Energy levels of ^{87}Rb

The next phase, called *interrogation*, involves microwave power and it is independent from the "optical" domain. Microwave power is divided into two time pulses so that the transition $F=2 \rightarrow F=1$ is probed (blue curve figure 1.5). This is the phase during which the local oscillator frequency is compared to the atomic clock frequency by means of Ramsey interferometry [11].

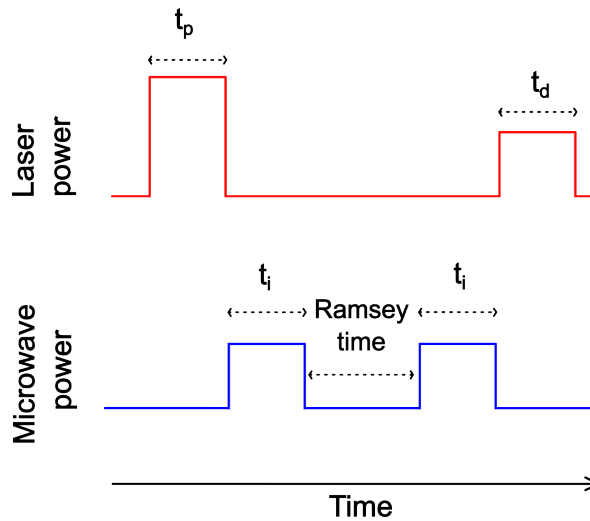


Figure 1.5: Ramsey scheme

After the *interrogation* a distribution of atoms in level $F=2$ is generated; it depends on the characteristic of the microwave pulses, it is called Ramsey pattern. In order

to obtain a pattern with narrow fringes, Ramsey time (fig. 1.5) between pulses should be chosen as large as possible [12]. In figure 1.6 a Ramsey fringe curve is presented, centered at the resonance frequency of the rubidium.

In the last phase, *detection*, the population of atoms in the level $F=2$ of the ground state is probed by observing the light absorption. The laser intensity will be a point of the curve 1.6, which means that by changing microwave detuning value, *detection* operation allows the control system to detect the central natural frequency. This phase is responsible for the correction that should be applied to local oscillator which generates the microwave frequency pulse during the Ramsey interaction time. The corrections to the quartz oscillator in a closed feedback-loop system results in the final output frequency of 10 MHz.

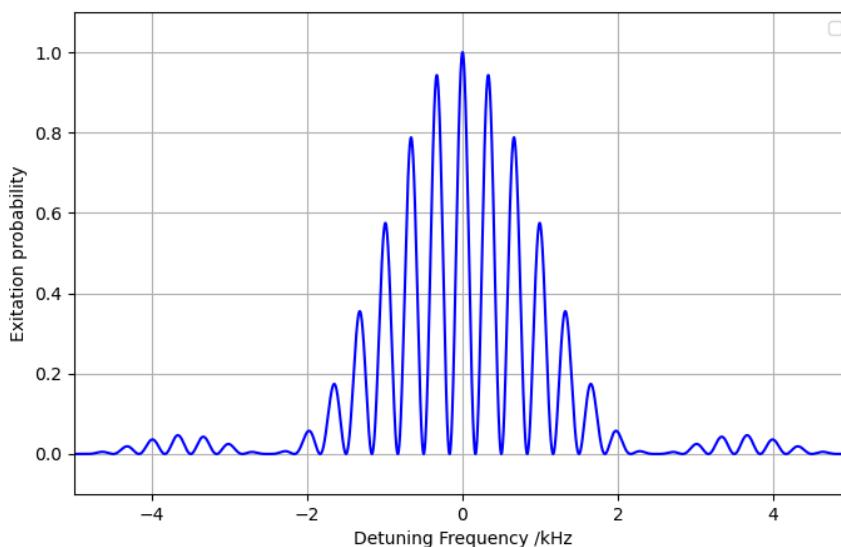


Figure 1.6: Example of a Ramsey-fringe patterns dependent on the microwave detuning, calculation follows the theory developed in [13]. This plot is centered at the natural frequency of the rubidium shifted due to the buffer gas.

POP clocks are an relatively complex system that for simplicity can be organized in 3 fundamental subsystems: optics, physics, electronics (1.7).

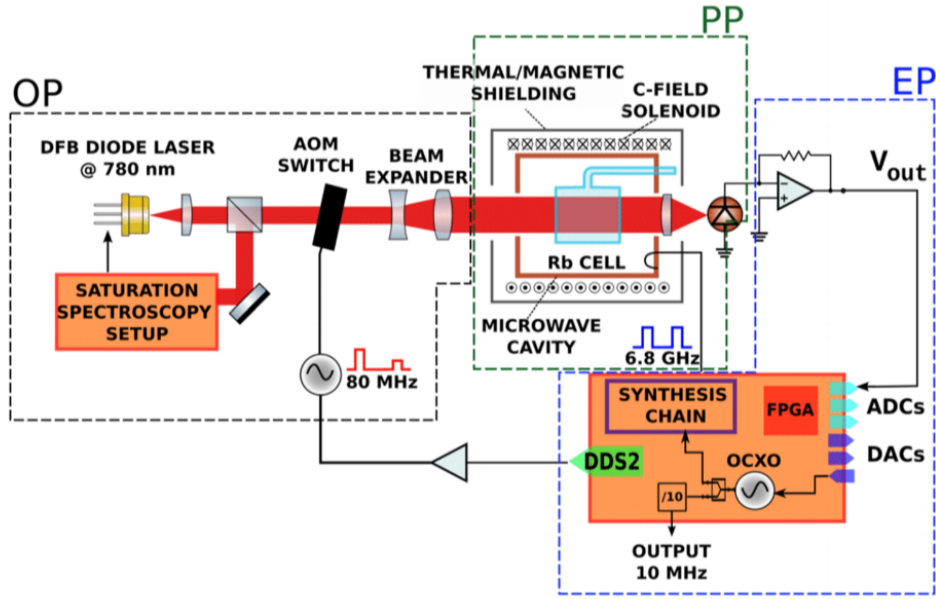


Figure 1.7: POP schematic, taken from [14]. Dashed frames include optics (OP), physics (PP) and electronics (EP) subsystem

The precision of this complex device relies on the tuning of the local oscillator after the interrogation phase of the vapor cell. There are some measurable physical quantities that affects with unwanted noise the clock frequency such as temperature, relative humidity, barometric pressure, laser noise ecc [15].

Vapor cells are filled with the target atom (rubidium) and a buffer gas used to narrow the resonance line by confining the Rb atoms in order to reduce wall collisions [1]. Typical gases are Ne, Ar, Kr. Atoms perform a Brownian motion, as they collide with the buffer gas. This reduces the average speed, effectively eliminating the Doppler effect, a mechanism known as Dicke narrowing [16]. Atoms can undergo thousands of elastic collisions with the buffer gas before losing their internal state coherence. In this way, the atomic clock cycle can be increased by orders of magnitude, from microseconds to milliseconds. However, buffer-gas collision also have a drawback: the introduction of an average net shift in the clock transition, that is dependent on the pressure and temperature of the buffer gas. This enhances the environmental sensitivity of vapor-cell clocks. The shift can be either positive or negative, depending on the buffer-gas species [17]. Therefore, a mitigation strategy is to use a mixture of two buffer gases with opposite sign, to transforming the temperature sensitivity from linear to quadratic. The POP clock uses a mixture of Ar (positive pressure shift) and N_2 (negative pressure shift), with a total pressure of 25 Torr.

1.3 Error Signal Generation

The tuning process of the local oscillator ν_s to the center frequency of resonance ν_0 is achieved by the usage of a proper error function. The picture 1.8 presents a simplified version of a vapor-cell clock, where the feedback loop of the control system is controlled by the servo processing block and an acousto-optic modulator creates two windows of preparation and detection.

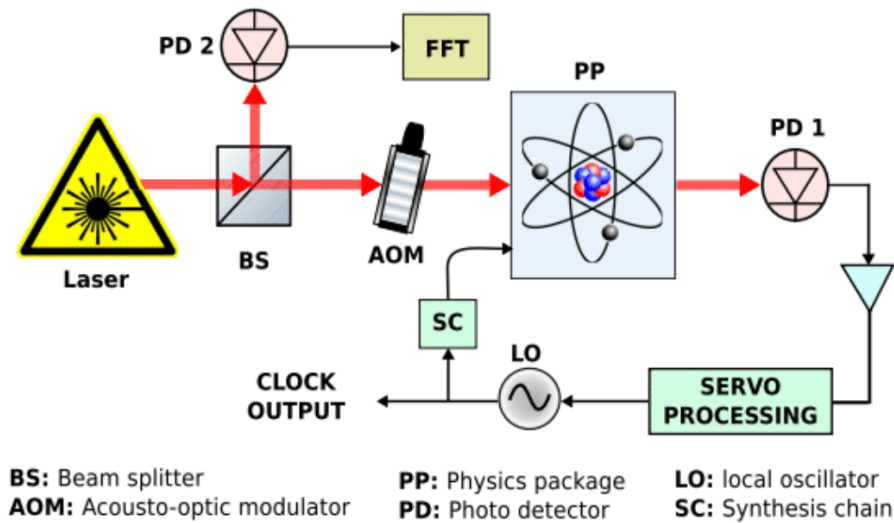


Figure 1.8: Simplification of a complete vapor-cell clock schematic. PD1 is the photodiode that detects the atomic signal, which is used to detect the clock transition, image was taken from [18]

The intensity of the laser observed by the photodiode in the detection phase is distributed (like showed in the previews section) on a the Ramsey fringe figure 1.6 [19]. The figure 1.9 represent a magnification of the central lobe of the fringes. By using a modulated wave, the microwave frequency is periodically shifted between $\nu_s + \delta\nu$ and $\nu_s - \delta\nu$, with ν_s equal to the oscillator frequency. This operation enables the collection of two absorption signal which contributes to the creation of error function.

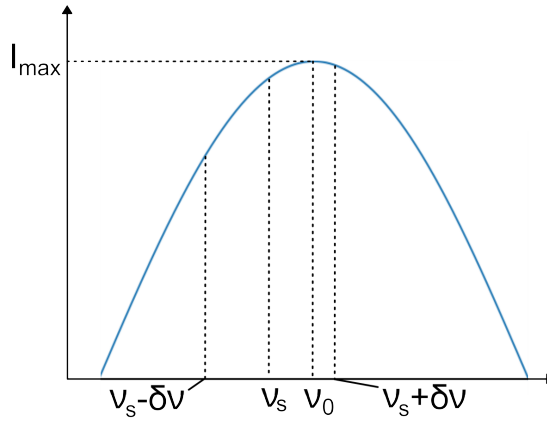


Figure 1.9: absorption function $I(\nu)$

By subtracting the intensities of the two received absorption samples in this modulation scheme makes possible to minimize the error function defined as $\Delta I = I(\nu_s + \delta\nu) - I(\nu_s - \delta\nu)$. In the figure 1.10 ΔI is represented as function of the difference between the resonance frequency and the frequency of the local oscillator. Maximum slope is reached when the clock is in tune.

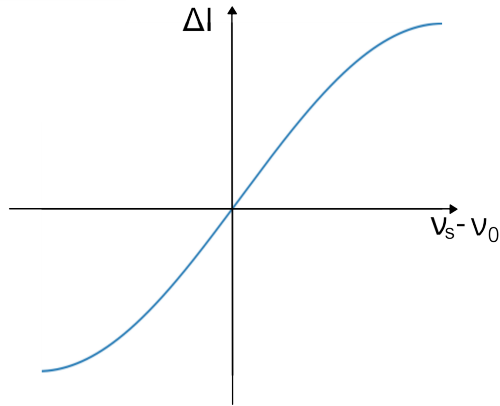


Figure 1.10: error function of ΔI , $\Delta I = I(\nu_s + \delta\nu) - I(\nu_s - \delta\nu)$

A well-known result related to the previous considerations is the equation 1.1 [19] which links the Allan variance (Appendix C) of the error to the intensity measured signal $I(\nu)$. For this relation it has been proved that the ADEV ($\sigma_y(\tau)$) has an inverse proportionality with the quality factor (Q). The factor σ^I is referred to the fluctuation of the signal.

$$\sigma_y(\tau) \propto \frac{1}{Q} \frac{\sigma^I(\tau = 1s)}{I_0} \frac{1}{\sqrt{\tau/s}} \quad (1.1)$$

A typical clock stability behavior $\sigma_y(\tau)$ is presented in the figure 1.11 [20].

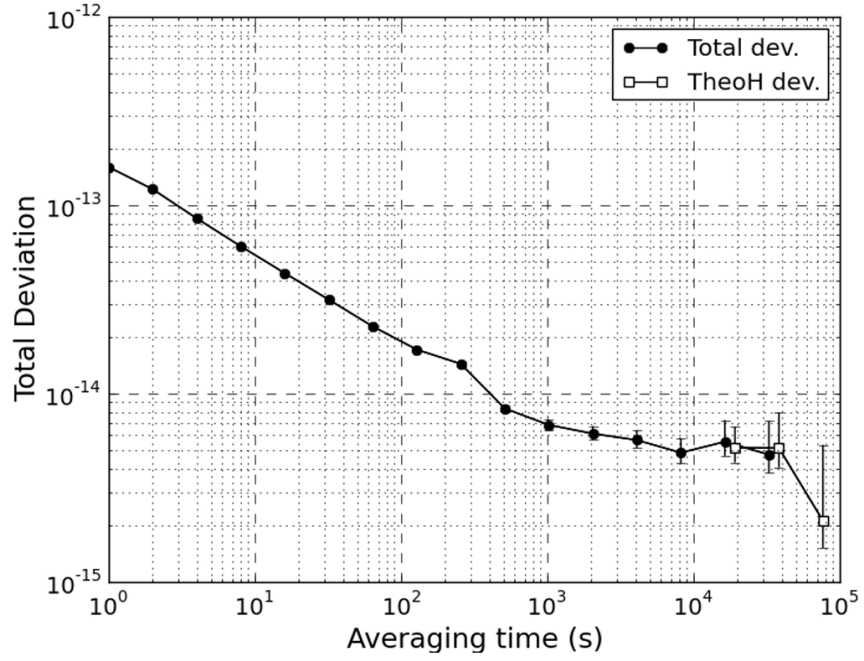


Figure 1.11: Clock stability of a POP clock (black line), taken from [20]

Chapter 2

Noise Contributions

This chapter presents a theoretical analysis of the possible noise contributions in an atomic vapor cell designed for absorption measurements. The focus is on identifying and characterizing the main noise sources that can affect the precision of the measurement, without considering direct experimental aspects. The signal of interest is the laser beam propagating through the atomic vapor cell, whose behavior is influenced by various physical processes fig. 2.1.

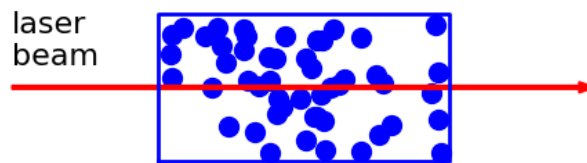


Figure 2.1: lateral view of the cell illuminated by a laser beam

The noise contributions can be categorized into four main types:

- *Laser technical noise:* This includes amplitude fluctuation due to instabilities in the laser source itself, this fluctuations can introduce correlated noise that affects the measurement process.
- *Shot noise:* This fundamental noise source arises from the discrete nature of photons. It sets a lower limit on the precision of optical measurements and is directly related to the intensity of the detected signal.
- *Atomic Brownian noise:* This noise originates from the thermal motion of atoms in the vapor cell. The random movement of atoms affects the absorption profile and can introduce fluctuations in the measured signal.

- *PM-AM noise*: This refers to noise arising from the coupling between phase modulation (PM) and amplitude modulation (AM) of the laser field. Even in the absence of intentional modulation, intrinsic noise in the laser system can lead to phase-amplitude conversion, contributing to unwanted signal fluctuations.

In this chapter, a theoretical discussion is provided for this noise contribution related to their fundamental origins and their impact on absorption measurements in atomic vapor cells.

2.1 Relative Intensity Noise of the Laser

The optical power of a laser is a crucial parameter that influences its performance. This power can be separated into two components: a constant average power, denoted as $\langle P \rangle$, and a fluctuating term, α , which varies over time during measurement. The fluctuating term, α , represents the relative intensity fluctuations. Thus, the optical power of the laser P can be expressed by the following formula:

$$P = \langle P \rangle (1 + \alpha) \quad (2.1)$$

As described in the equation, the laser's intensity spectrum is proportional to the square of the optical power. Therefore, it is possible to write the intensity spectrum as shown in equation 2.2:

$$S_P(f) = \langle P \rangle^2 S_\alpha(f) \quad (2.2)$$

Here, $S_\alpha(f)$ refers to the power spectral density of the relative intensity fluctuations, α . For a laser diode, the optical power is directly proportional to the photocurrent I received by a photodiode. By defining I as the photocurrent and I_0 as its DC value, the laser's Relative Intensity Noise (RIN) can be introduced. The relationship between the optical intensity spectrum and the Laser RIN is expressed by the following equation:

$$RIN = \frac{S_I(f)}{I_0^2} = \frac{S_P(f)}{\langle P \rangle^2} = S_\alpha(f) \quad (2.3)$$

Like most semiconductor devices, laser diodes exhibit a flicker amplitude noise. When properly biased above the threshold current, this noise becomes independent of the laser's emitted optical power. This $1/f$ noise is generally most significant at lower frequencies (below 100 kHz) [21], and it can be mitigated by using a modulator. In GaAlAs lasers, the origin of $1/f$ noise is often linked to fluctuations in spontaneous emission or variations in the laser gain within the cavity, contributing to the overall noise characteristics of the laser [22].

2.2 Shot Noise

Shot noise is caused by the discrete nature of photons which causes a random fluctuation on the surface of the photodiode. This noise is detected together with other contribution and by his nature its a power dependent factor.

This noise contribution can be modeled by the product of the energy of a photon and the optical power.

$$S_{shot} = 2h\nu \langle P \rangle \quad (2.4)$$

In the equation 2.4, ν is the frequency, $\langle P \rangle$ is the mean optical power and h is the Plank constant. The equation of the photocurrent is the following.

$$I = \eta P \quad (2.5)$$

The factor η is the Responsitivity. of the photodiode and " I " is the photocurrent corresponding to the specific optical power. Typical responsivity for silicon detectors in the visible and near-infrared (NIR) laser are in the range 0.5 to 0.8 A/W. For the current application NIR laser will be used which have the lowest responsivity.

2.3 Brownian Noise

Brownian noise, also known as Brownian motion noise, refers to a specific type of noise signal originally introduced to describe the random movement of particles suspended in a fluid. First observed by Robert Brown in 1827 while studying the motion of pollen grains in water, this model can also be applied to various other physical phenomena.

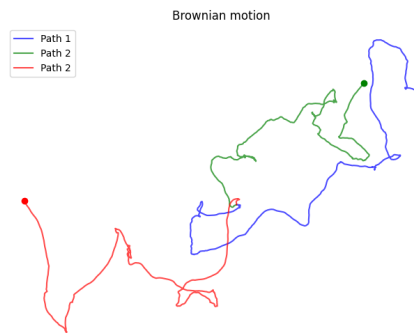


Figure 2.2: Simulation of three pollen particles suspended in water that covers a Brownian motion; initial position $(x,y) = (0,0)$; initial speed $(v_x,v_y)=(0,0)$

Rubidium atoms behave like any small particles suspended in a fluid when they are confined in a cell with a buffer gas. Atomic motion is the cause of an intensity noise for laser signal which transit in the atomic medium.

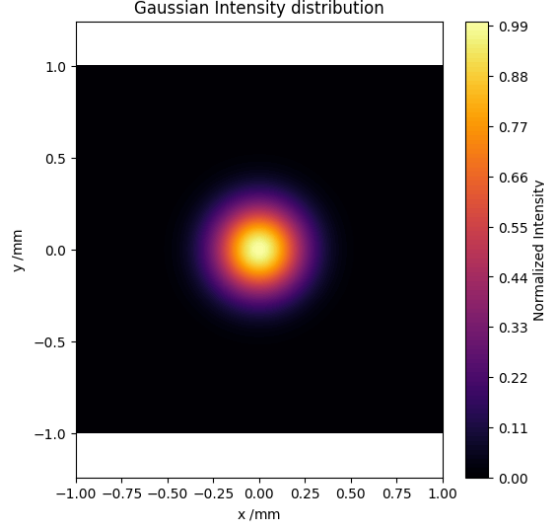


Figure 2.3: Laser intensity distribution for $w = 0.34$ mm

In the figure 2.3 is showed a Gaussian graphical representation of the intensity profile of a laser beam. By introducing the factor w for the beam radius, the relationship between position and light intensity $I(x, y)$ is expressed in equation 2.6.

$$I(x, y) = I_0 e^{-2\frac{x^2+y^2}{w^2}} \quad (2.6)$$

The optical power of a laser which shines an atomic vapor is function of the electrical power $\mathcal{E}(x, y)$ and the Lorentzian function like expressed by formula 2.8. The relation presents ω which is fixed to the resonance frequency of the rubidium for the D_2 transition, μ_{Rb} instead is the dipole moment of the atom [23].

$$\mathcal{P}(t) = \frac{\mu_{Rb}^2 \omega}{4\hbar} |\mathcal{E}(x, y)|^2 \frac{\Gamma}{(\Delta\omega + k\nu_z)^2 + \Gamma^2} \quad (2.7)$$

In the equation 2.7 it is present a Lorentzian multiplicative coefficient which is related to the absorption of the atomic medium at different frequencies. The relationship between $\mathcal{E}(x, y)$ and laser intensity $I(x, y)$ is presented in the equation 2.8, 2.9.

$$\mathcal{E}(x, y) = \mathcal{E}_0 e^{jkz - i\omega t} \quad (2.8)$$

$$I_0 = \frac{1}{2} c \epsilon_0 \mathcal{E}_0^2 \quad (2.9)$$

If the laser perfectly centered in the peak of the rubidium absorption curve the power has a negligible Lorentzian behavior simplifying the general description.

$$\mathcal{P}(t) \approx \sigma I(x, y) \quad , \quad \sigma = \frac{2\mu_{Rb}^2 \omega}{c \epsilon_0 \hbar \Gamma} \quad (2.10)$$

$$\mathcal{P}(t) \approx \sum_j^n \sigma I(x_j(t), y_j(t)) \quad (2.11)$$

The formula 2.10 isolates the two main contribution of the power, σ , the standard formula for the photon absorption cross section and I , laser intensity. Every atom of the vapor cell has the same σ and shone with the same laser intensity so that a summation of every power contribution is needed to estimate the total power. The equation 2.11 shows the result of the superposition of n (atoms per volume) atoms using letter j as atomic index. Linking the definition of the power spectrum ($S_{Br}(f)$) to the simplified $\mathcal{P}(t)$ equation 2.12 is obtained [23].

$$\begin{aligned} S_{Br}(f) &= \frac{1}{T_{meas}} \int_0^{T_{meas}} |\mathcal{P}(t)| e^{-j\omega t} dt = \\ &= \frac{1}{T_{meas}} \left| \sum_j^n \int_0^{T_{meas}} \sigma I(x_j(t), y_j(t)) e^{-j\omega t} dt \right| \end{aligned} \quad (2.12)$$

The equation 2.12 contains like before the atomic index j where every atom perform a random walk in free space independently. By using the property of random walk the final approximate expression is obtained.

$$S_{Br}(f) \approx \frac{2n\sigma^2 L P^2 D}{\pi^3 w^4} \frac{1}{f^2} \quad (2.13)$$

In the equation 2.13 [23] the PSD of the Brownian Noise is presented; its main contributions are: σ^2 absorption cross-section, L length of the cell, w diameter of a beam, P optical power, D diffusion coefficient, n atoms per volume. The main consequences of this formula is that Brownian noise has a spectrum of f^{-2} and it is constant in a controlled environment (stable temperature).

Due to the inverse proportionality with the laser beam diameter the Brownian noise is also called **transit noise** [24] because, the effect of absorption of a beam more concentrated has a higher impact on the absorption measure. A smaller beam (lower w) causes effect of atomic interruption of the laser beam which increases the atomic noise ($S_{Br}(f) \propto 1/w^4$).

2.4 PM-AM Noise

Generally, lasers are manufactured with a narrow bandwidth to ensure stable operation. However, the emitted frequency can be affected by various noise sources, leading to fluctuations in phase and amplitude. One of the main consequences of phase noise is its potential conversion into intensity noise, known as PM-AM noise conversion. The phase instability of the laser beam causes a frequency fluctuation that, when passing through an absorbing medium such as an atomic vapor cell, can be converted into amplitude modulation. This occurs because the laser's frequency noise interacts with the medium's absorption profile, leading to variations in transmitted intensity. Defining η_L as the laser frequency and η_{L0} as the frequency at which the absorption curve is centered, the absorption line shape of the atomic medium through which the laser is passing can be expressed as $L(\nu_L - \nu_{L0}) = I(\nu_L)/I_0$ [25]. Furthermore, if $\delta\nu_L$ represents the laser frequency fluctuation, the PM noise can be converted into AM noise with the heuristic formula 2.14. This equation expresses how the intensity noise is proportional to the frequency noise weighted by the slope of the absorption profile.

$$\frac{\delta I(\nu_L)}{I_0} = \delta\nu_L \cdot \left| \frac{dL}{d\nu_L} \right| \quad (2.14)$$

Like showed in the Figure 2.4 the maximum output noise can be reached if the laser is tuned in the maximum slope points of the absorption curve. Consequently, operating a laser near these regions can significantly impact the stability of the optical system.

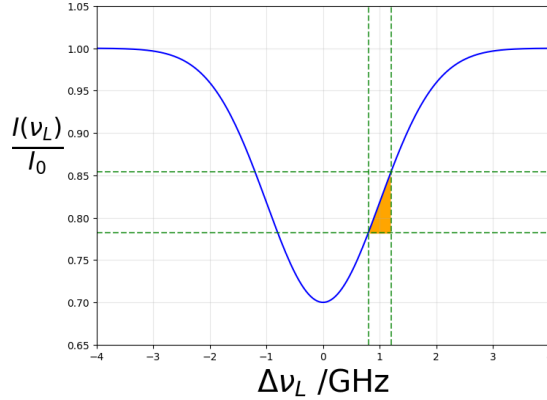


Figure 2.4: Phase noise example in a generic rubidium absorption profile, y-axis represents relative absorption $L = I(\nu_L)/I_0$

Chapter 3

Cross-correlation

Cross-correlation is a fundamental mathematical operation used to quantify the similarity between two signals. This technique is particularly valuable in scenarios where identifying correlated fluctuations between datasets is crucial, such as in noise analysis. In optical systems designed for atomic noise measurements, cross-correlation methods play a key role in enhancing signal detection and filtering out unwanted disturbances. This chapter provides a comprehensive mathematical overview of the cross-correlation operation, followed by an exploration of its implementation in optical schemes for atomic noise measurement. Specifically, it is structured as follows:

- Section 3.1 and Section 3.2 introduce the fundamental mathematical aspects of cross-correlation and the statistical tools associated with it.
- Section 3.3 explores the different types of cross-correlation estimators that can be implemented.
- Section 3.4 presents optical schemes inside which cross-correlation techniques are applied with the purpose of detecting atomic noise of a rubidium vapor-cell in order to distinguish it from spurious contribution.

3.1 Basics

A powerful method for characterizing amplitude modulation (AM) noise allows the measurement of the power spectral density (PSD) of a specific device under test (DUT), even in the presence of additional additive noise contributions. Unlike traditional PSD measurements that typically involve single-channel acquisition, this method uses two channels and applies cross-spectral processing after acquisition. The experimental setup is illustrated in Figure 3.1. The DUT presents a common-mode noise, $c(t)$, which is measured by two channels, A and B. These channels also capture the instrument's front-end additive noise contributions, $a(t)$ and $b(t)$

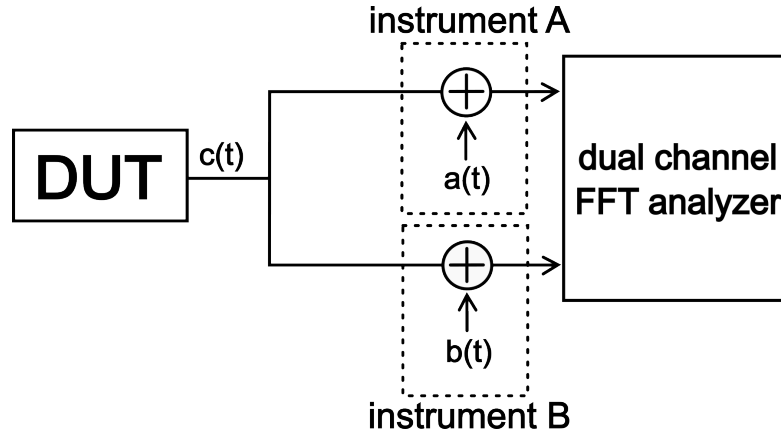


Figure 3.1: Basic cross-spectrum measurement

The figure 3.1 is a representation of the experimental setup. The DUT presents a common-mode noise $c(t)$ measured with two channels A and B of an instrument that offers its front-end analog noise additive contribution $a(t)$ and $b(t)$.

$$x(t) = c(t) + a(t) \quad (3.1)$$

$$y(t) = c(t) + b(t) \quad (3.2)$$

The signals $x(t)$ and $y(t)$ are the final inputs to the measurement system. After simultaneous acquisition from both channels, the cross-spectrum of the two channels can be computed as follows:

$$\begin{aligned} \langle S_{yx}(f) \rangle_m &= \frac{2}{T} \langle Y(f)X(f)^* \rangle_m = \\ &= \frac{2}{T} \langle [C(f) + B(f)][C(f) + A(f)]^* \rangle_m = \end{aligned} \quad (3.3)$$

Expanding this expression it is obtained:

$$= \frac{2}{T} [\langle C(f)C(f)^* \rangle_m + \langle C(f)A(f)^* \rangle_m + \langle B(f)C(f)^* \rangle_m + \langle B(f)A(f)^* \rangle_m] = \quad (3.4)$$

$$\langle S_{yx}(f) \rangle_m = \langle S_c(f) \rangle_m + O(\sqrt{1/m}) \quad (3.5)$$

Here, m represents the number of averaged spectral samples used in the computation of the cross-spectrum. As m increases (i.e., as more samples are taken), the noise contributions from uncorrelated sources become progressively smaller, following a $1/m$ convergence rate. This means that, to obtain a reliable and accurate measurement of the PSD, a large number of samples (m) is required. The term $\langle C(f)C(f)^* \rangle_m$ corresponds to $\langle S_c(f) \rangle_m$, which represents the power spectral density of the common-mode noise (Wiener-Khinchin theorem). The other terms in the equation are uncorrelated, and their contributions decrease with a $\sqrt{1/m}$ trend as m increases, making them progressively less significant.

However, two main issues arise in this measurement setup ([26]):

- convergence follow the $\sqrt{1/m}$ trend, which means that a large number of samples is required to effectively reduce the impact of uncorrelated noise and obtain high-quality measurements.
- Correlated noise sources, such as cross-talk and environmental fluctuations, cannot completely be eliminated by this method. These sources may still affect the accuracy of the results and must be carefully managed or mitigated in the experimental setup.

3.2 Statistical Tools

The cross-spectrum of two signals is equal to the Fourier transform of the cross-correlation between them [27].

$$S_{yx}(f) = \mathfrak{F}\{R_{yx}(\tau)\} \quad (3.6)$$

The equivalence rules of convolution allows a further simplification with correlation because the Fourier transform of a cross-correlation $R_{yx}(\tau)$ is equal to $Y(f)X^*(f)$. Usually signals are acquired in a huge number of windows to estimate the Expected value of the DUT and it's standard deviation.

$$E\{S_{yx}(f)\} = E\{Y(f)X^*(f)\} \quad (3.7)$$

Frequency for the purposes of this analysis can be considered fixed at a specific value, in order to consider $S_{yx}(f = f_0)$ a random variable (3.2).

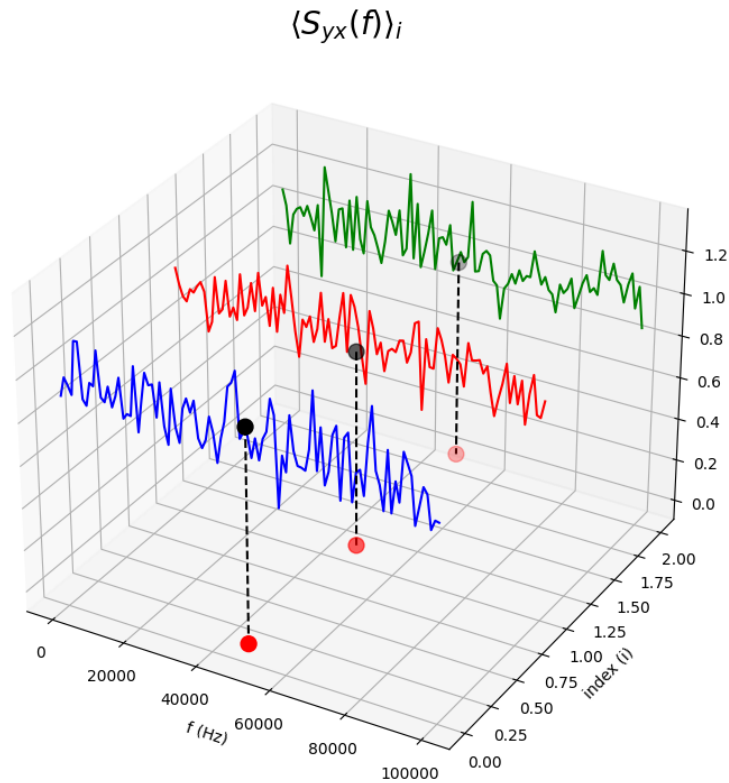


Figure 3.2: 3D visualization of the selection of a specific frequency in the sequence of $\langle S_{yx} \rangle_i$

The expected value can be estimated performing the average on a selected group of m samples, for the specific frequency. This procedure can be easily performed assuming that this process is ergodic. It is possible to interchange time statistics and ensemble statistics.

$$E\{S_{yx}(f)\} = \langle S_{yx} \rangle_m = \langle YX^* \rangle_m \quad (3.8)$$

After the isolation of real and imaginary parts (eq. 3.9) it is possible to obtain the modulus of the product of the two Fourier transforms (eq. 3.10).

$$\langle S_{yx} \rangle_m = \langle (Y_R X_R + Y_I X_I) + i(Y_I X_R - Y_I X_R) \rangle_m \quad (3.9)$$

$$|\langle S_{yx} \rangle_m| = \sqrt{[\langle Y_R X_R + Y_I X_I \rangle_m]^2 + [\langle Y_I X_R - Y_I X_R \rangle_m]^2} \quad (3.10)$$

$$|\langle S_{yx} \rangle_m| = \sqrt{[\langle Z_R \rangle_m]^2 + [\langle Z_I \rangle_m]^2} \quad (3.11)$$

The equivalence showed in the equation 3.11 is particularly important because there is an important property of statistics that can be used to obtain the distribution of the random variable $|\langle S_{yx} \rangle_m|$. Given a $R(\sigma)$ a Rayleigh distribution it is possible to define the following property:

$$R(\sigma) = \sqrt{X^2 + Y^2}$$

Assuming that X and Y are two independent zero-mean Gaussian random processes with the same variance equals to σ^2 . The random process $|\langle S_{yx} \rangle_m|$ has a Rayleigh distribution if the following assumptions are true:

1. The real and the imaginary part Z_I and Z_R are random variables with Gaussian distribution.
2. Z_I and Z_R are statistically independent with the same variance.
3. The random variables Z_I and Z_R evaluated in different frequency slots are statistically independent form the current one.

After the imposition of a normalization on X and Y in order to obtain a variance equal to one ($\text{VAR}\{X\} = \text{VAR}\{Y\} = 1$) and the assumption of their Gaussian distribution (for the central limit theorem), it is possible to build a table of all parameters (tab. 3.1).

$\text{VAR}\{X\}$	1	$\text{VAR}\{Y_R X_I\}$	1/4
$\text{VAR}\{Y\}$	1	$\text{VAR}\{Y_I X_I\}$	1/4
$\text{VAR}\{Y_R X_R\}$	1/4	$\text{VAR}\{Y_I X_R\}$	1/4

Table 3.1: Table of values of the variances referred to the random process X and Y

Z_I and Z_R are two Gaussian distribution with $\sigma^2 = 1/2m$. The equation 3.11 proves that $|\langle S_{yx} \rangle_m|$ has a Rayleigh distribution with an expected value equals to $\sigma\sqrt{\pi/2}$ and variance equals to $\sigma^2(2 - \pi/2)$. Substituting the $\sigma^2 = 1/2m$ in the Rayleigh equations retrieves the following values:

Standard deviation of $ \langle S_{yx} \rangle_m $	$\sqrt{(1 - \frac{\pi}{4}) \frac{1}{m}}$
Average of $ \langle S_{yx} \rangle_m $	$\sqrt{\frac{\pi}{4m}}$

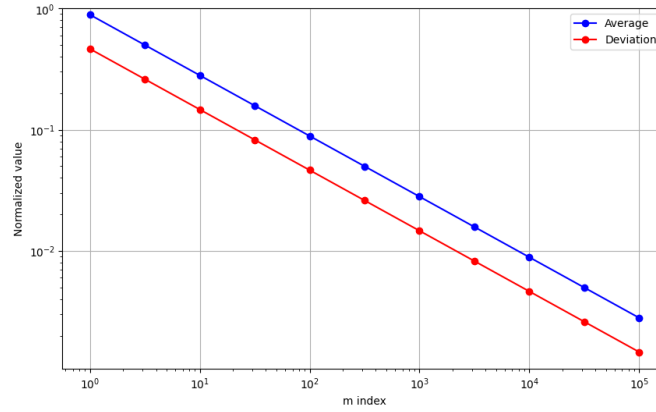


Figure 3.3: Average and standard deviation at the increasing of "m", averaging factor

Only in absence of DUT noise the reduction of Average follows this trend this means that after the suppression of noise of interest is will be stable.

3.3 Cross-spectrum Estimators

Common estimation of cross-correlation spectrum involves the absolute value of the complex quantity $\langle S_{yx} \rangle_m$. This kind of estimator is commonly implemented by instruments and computational tools. The risk of the usage of the absolute value is the waste of information of the complex spectrum function in frequency domain. Cross-spectrum (CSD) differently from power spectrum (PSD) hides more information in the real and imaginary component and their signs.

Starting from the usual set of equations (eq. 3.12, 3.13) $x(t)$ and $y(t)$ are of two input signals and $c(t)$ is the DUT that cross-correlation should allow to emerge.

$$x(t) = c(t) + a(t) \quad (3.12)$$

$$y(t) = c(t) + b(t) \quad (3.13)$$

The Fourier transform of $x(t)$ and $y(t)$ is divided into a real and an imaginary part (eq. 3.14) in order to observe cross-correlation operation in the complex space.

$$X = (A'' + iA'') + (C' + iC'') \quad \text{and} \quad Y = (B' + iB'') + (C' + iC'') \quad (3.14)$$

In fact, the mean of the cross-spectrum with index m (number of averages) (3.15) can be splitted into his real (eq.3.16) and imaginary part (eq.3.17) because both, Fourier and average operation, are linear operators.

$$\langle S_{yx} \rangle_m = \frac{2}{T} \langle YX^* \rangle_m = \frac{2}{T} \langle (Y' + iY'') \times (X' - iX'') \rangle_m \quad (3.15)$$

$$\Re\{\langle S_{yx} \rangle_m\} = \frac{2}{T} \{ \langle B'A' + B''A'' \rangle_m + \langle B'C' + B''C'' \rangle_m + \langle C'A' + C''A'' \rangle_m + \langle (C')^2 + (C'')^2 \rangle_m \} \quad (3.16)$$

$$\Im\{\langle S_{yx} \rangle_m\} = \frac{2}{T} \{ \langle B''A' + B'A'' \rangle_m + \langle B''C' - B'C'' \rangle_m + \langle C''A' - C'A'' \rangle_m \} \quad (3.17)$$

The easiest cross-spectrum estimator, expressed with \widehat{S}_{yx} , the magnitude of $\langle S_{yx} \rangle_m$ presents some limitations.

$$\widehat{S}_{yx} = |\langle S_{yx} \rangle_m| = \sqrt{\Re\{\langle S_{yx} \rangle_m\}^2 + \Im\{\langle S_{yx} \rangle_m\}^2} \quad (3.18)$$

Like showed in the equation 3.17, the imaginary part of $\langle S_{yx} \rangle_m$ does not contribute in estimating the PSD ($S_{c,c}$) of a correlated noise contribution($c(t)$). For this reason the magnitude of $\langle S_{yx} \rangle_m$ is not considered the optimum estimator [28] . The real part of the average measured cross-spectrum (eq. 3.19) is instead a powerful method which contains more information with some manageable drawbacks.

$$\widehat{S}_{yx} = \Re\{\langle S_{yx} \rangle_m\} \quad (3.19)$$

This estimator can reach negative values which can be a problem if the y-axis is in a logarithmic scale (dB). In this case understanding the portion of the spectrum which satisfy the relation $\Re\{\langle S_{yx} \rangle_m\} < 0$ is necessary and, furthermore, very interesting. In presence of negative spectrum values in order to plot them in a decibel chart is necessary to invert their sign. These strange ranges should also be considered as warning points because they reveal the presence of an anticorrelated noise contribution.

3.3.1 Artifacts in the Cross-correlation Spectrum

Sometimes the cross-spectrum profile contains some interesting artifact which reflects particular characteristic of the noise contributions [29] *. Considering this two channel acquisition with $x(t)$ and $y(t)$ as input in time domain

$$\begin{aligned} x(t) &= a(t) + c(t) + d(t) \\ y(t) &= b(t) + c(t) + d(t) \end{aligned} \quad (3.20)$$

Where $a(t), b(t)$ and $c(t)$ are White Gaussian noises instead $d(t)$ is a flicker noise. Their single PSD is presented in the figure 3.4. Another composition of noise can be introduced now, $\tilde{y}(t)$. This noise (eq.3.21) is similar to $y(t)$ but has an anticorrelation for what involves $d(t)$ (the sign is changed).

$$\tilde{y}(t) = b(t) + c(t) - d(t) \quad (3.21)$$

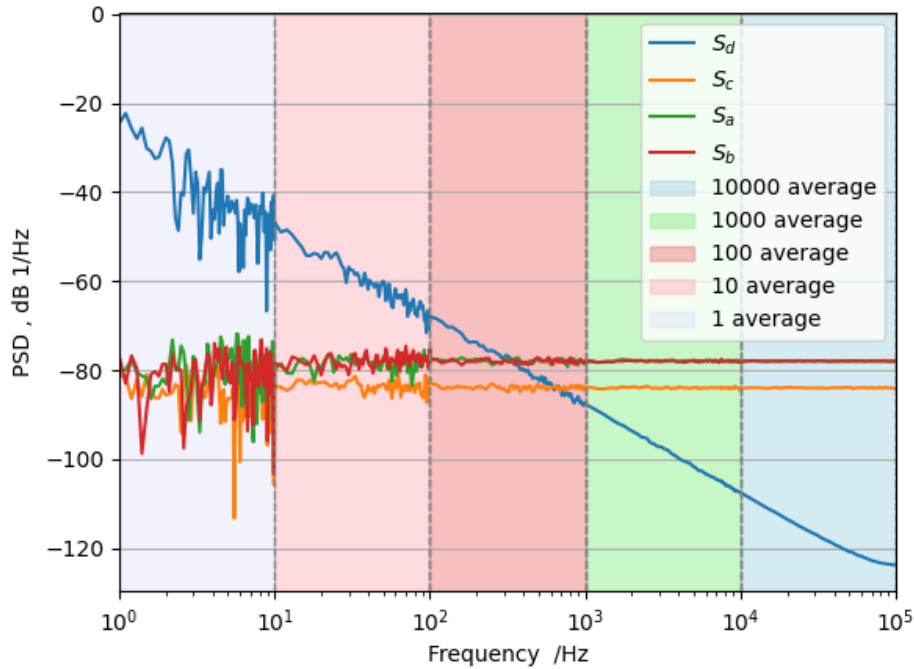


Figure 3.4: Single spectrum contribution for $a(t)$, $b(t)$, $c(t)$, $d(t)$ of the equation 3.20

*plot and diagram showed in this section are results of the python code in appendix B

Figure 3.5 present the real part of the cross-spectrum between $x(t)$ and $y(t)$ (blue curve) and the real part of the cross-spectrum between $x(t)$ and $\tilde{y}(t)$ (orange and red curve). The two cross-correlation spectrum are similar each other but for what concerns $\Re\{\langle S_{x,\tilde{y}} \rangle_m\}$ it is possible to notice a "notch" [30] at the frequency of 1 kHz. This artifact separates the range of the spectrum in which the Real part is positive from the negative one. This behavior is linked to the inversion of the phase caused by the anticorrelated noise component $d(t)$ which is consistent in the lower frequency ($[1-10^3]$ Hz), this phenomena caused the "notch".

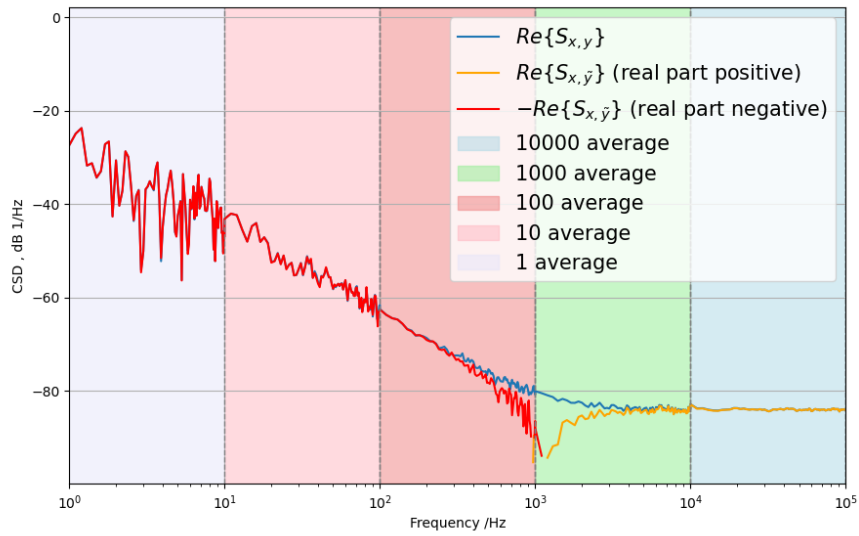


Figure 3.5: Cross-correlation between x and y compared with x and the version of y which contains an anticorrelated contribution \tilde{y} (eq. 3.21)

The behavior presented here is a proof of concept of what happen when the optimum estimator is employed and what kind of information it holds.

3.4 Experimental Test Bench for Measuring the Intensity Noise Contributions

It is possible to utilize the cross-correlation block, described in the previous sections, to selectively isolate noise contributions in the context of atomic absorption measurements. The noise contributions, previously analyzed in detail in Chapter 2, will now be categorized as follows:

- S_A : Atomic noise originating from the interaction between the laser beam and the atomic medium, which represents the primary signal of interest in these measurements.
- $S_{PM/AM}$: Noise due to phase-to-amplitude (PM/AM) conversion.
- S_T : Amplitude technical noise introduced by the laser.
- N : Shot noise, originating from quantum fluctuations in the photon number.
- E : Electronic noise generated by the acquisition system and photodiodes front-end.

The single channel absorption measure exhibit a combination of all noise contribution distributed along the measurement chain like depicted in the image 3.6.

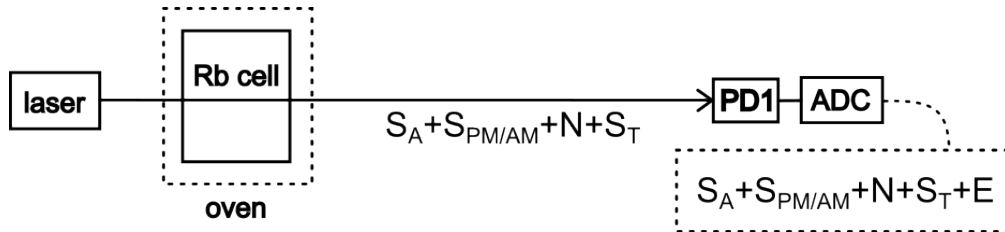


Figure 3.6: Noise contribution in a simple acquisition absorption setup. In the figure: arrow represents a laser beam, PD1 is a photodiode, ADC is a analog to digital converter.

Figure 3.7 illustrates a typical acquisition schematic. The laser beam is split into two paths, with each path affected by shot noise (N_1 and N_2) and electronic noise (E_1 and E_2). The laser's technical noise, represented by S_T , is common to both channels. As a result, the cross-correlation block allows this noise to be separated from the other noise contributions [26].

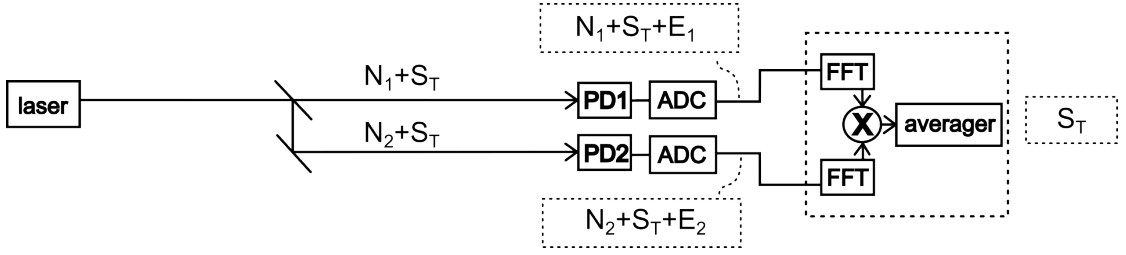


Figure 3.7: measurement setup for laser technical noise. In the figure: arrow represents a laser beam, PD1 and PD2 are photodiodes, ADCs are the channels of the analog to digital converter.

In the picture 3.8, like the previous example, every channel presents its own electronic noise (E) and shot noise (N). Common mode noise is made of two contributions: laser technical noise (S_T), atomic noise (S_A) and PM/AM noise conversion ($S_{PM/AM}$). The cross-correlation between the acquired signals coming from the two photodiodes PD1 and PD2 decrements the uncorrelated contributions of electronic and shot noises. This setup estimates the spectrum of the composition of noise of common mode contribution: $S_T + S_A + S_{PM/AM}$.

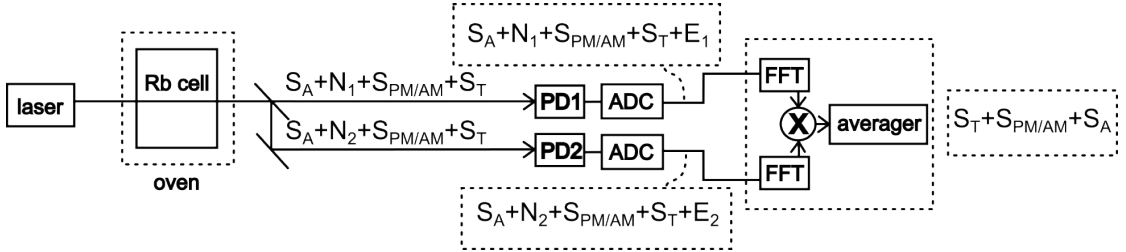


Figure 3.8: measurement setup for rubidium atomic noise and technical laser noise. In the figure: arrow represents a laser beam, PD1 and PD2 are photodiodes, ADCs are the channels of the analog to digital converter.

As shown in Figure 3.7, using a shared laser source inherently results in common-mode laser noise. The standard approach to rejecting common-mode noise is the use of differential amplifiers, a well-established electronic principle that is extended to optical setups. This principle is applied in the schematic shown in Figure 3.9[31].

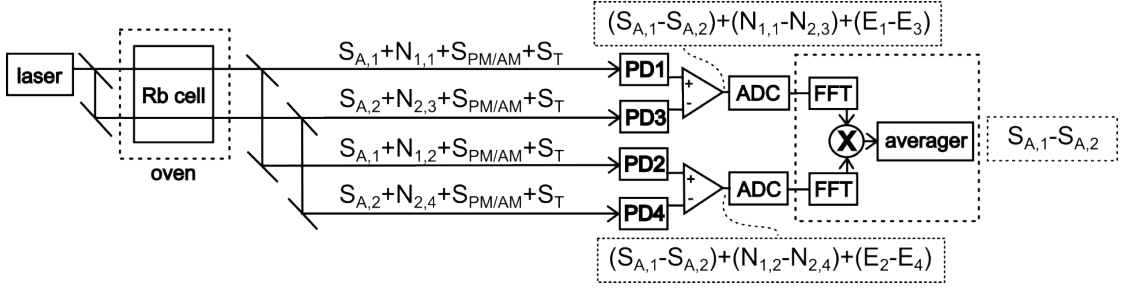


Figure 3.9: measurement setup for rubidium atomic noise. In the figure: arrow represents a laser beam, PD1-PD4 are 4 photodiodes, ADCs are the channels of the analog to digital converter.

Laser technical noise and its PM/AM conversion are suppressed thanks to the two operational amplifiers. In order to avoid the subtraction of Brownian noise, the atomic contribution is divided into two independent paths; two parallel laser rays illuminate the vapor-cell. These two independent paths bring two uncorrelated atomic contributions, their difference emerges from the cross-correlation block. Moreover, by subtracting the signals from the two channels, PM/AM noise conversion is also mitigated, as it primarily affects both paths in a correlated manner. Finally, as in the previous setups, the cross-correlation technique is applied to further reduce uncorrelated noise contributions, specifically electronic noise and shot noise, leading to an overall improvement in measurement sensitivity and accuracy.

Chapter 4

Instruments Characterization

This chapter presents the technical and functional characteristics of the instruments employed for the experimental measurements. In particular, the analysis focuses on the data logger, photodiodes and laser diode. The relevant parameters have been extracted from the datasheets to highlight the key characteristics and provide a clearer understanding of the instruments' performance. Every tool used in chapter 5 and 6 for observation is here presented.

4.1 DAQ

Heavy data processing operations usually rely on fast and high-resolution acquisition tools. Fundamental specification for the scope of this work is the possibility of a Multichannel acquisition. The selected instrument, Keysight DAQ970A (fig. 4.1), presents desired specifications and a low quantization noise. Furthermore due to its high data-rate it's possible to exchange data with the PC by the means of the SCPI (Standard Commands for Programmable Instruments) protocol thanks to the commonly used library PYVISA available for the Python programming language.

This Data logger has 4 independent slots that can mount different modules in order to extend the instrument elaboration and acquisition features. The selected expansion board is the DAQM909A (fig. 4.1) a module with a 24 bit Delta-Sigma A/D converter and a maximum of 4 channels (tab. 4.1).



Figure 4.1: Keysight DAQ970A instrument, photo taken from [32]

ADC per channel	800 kSa/s @ 24-bit
Range (Hi, Lo Input to Earth)	0.3 Vpk, 1 Vpk, 3 Vpk, 18 Vpk
Range (Differential input)	0.6 Vpk, 2 Vpk, 6 Vpk, 36 Vpk
Input impedance (Hi or Lo to Earth)	1 M Ω 400 pF
Analog bandwidth (-3 dB)	125 kHz (measured)
THD (1 kHz)	-103 dB
THD (20 Hz-20 kHz)	-83 dB
Channel to Channel cross-talk (1 kHz)	-100 dB

Table 4.1: DAQM909A module features

The analog bandwidth is measured by observing the frequency response of the logger by means of a signal generator. The signal generator, connected to the instrument, provides sine waves at the various frequencies. The amplitude of the sinusoidal signal collected by the DAQ is showed creating the complete analog bandwidth plot (fig. 4.2). The y-axis in the figure (dB) is computed with a normalized logarithmic equation $20 * \log_{10}(\frac{V_{in}}{300mV})$ assuming that for the chosen input range the maximum amplitude of the sinusoidal signal is 300mV.

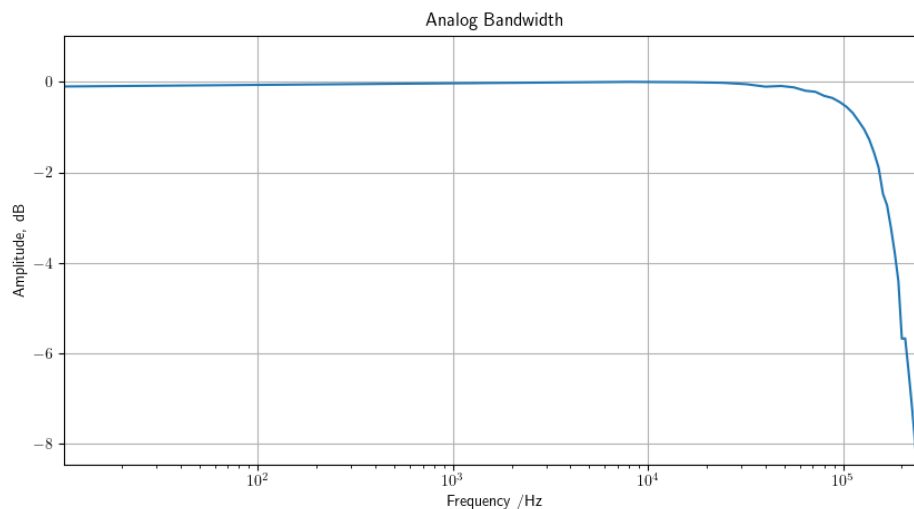


Figure 4.2: Keysight DAQ970A input gain bandwidth

Like shown in table 4.1, the producer declares a bandwidth of 125 kHz and this is confirmed also by the signal generator observations. The module DAQM909A is capable of changing its sample frequency without any aliasing protection for frequency lower than 125 kHz. Testing the absence of anti-aliasing filters on the analog front end it is an opportunity to better characterize the system. It is possible to define a procedure to detect the presence of an anti-aliasing filter with following steps:

- Sampling frequency is fixed to values lower than the input bandwidth declared by datasheet (e.g. 20kHz or 50 kHz).
- Input, a waveform generator, generates sines in the frequency range [1-100 kHz].
- Detection of the actual frequency of the incoming signal is performed by the means of the FFT through which is observed the position of the maximum peak in the frequency axis.

The figures 4.3 and 4.4 prove the point, no aliasing filter is provided by the instrument. X-axis (input frequency) represents the frequency of the input wave; y-axis (detected frequency) is the detected frequency of the signal.

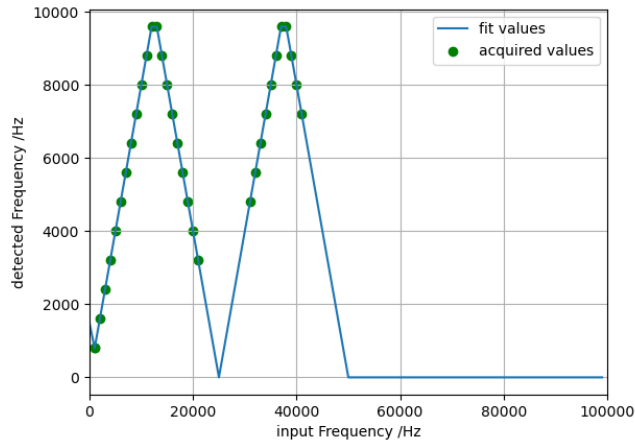


Figure 4.3: Aliasing effect when the sampling frequency is 20 kHz

Results show that if spectral contribution are not limited inside the selected bandwidth they can affect the signal and disturb it inside the measured frequency window. A way to avoid the aliasing input noise is the usage of an analog input filter. This solution is generally avoided to reduce an additive noise contribution offered by active input components.

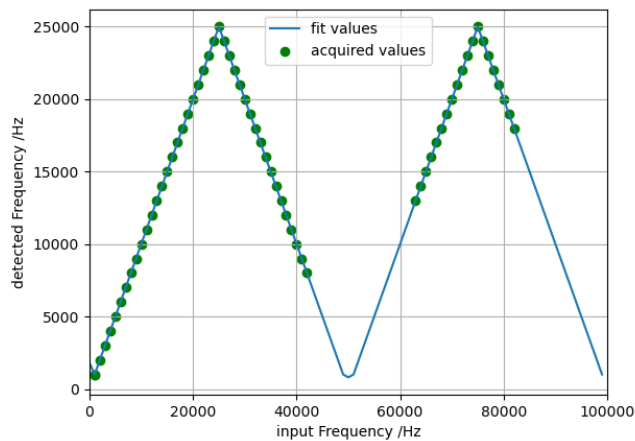


Figure 4.4: Aliasing effect when the sampling frequency is 50 kHz

Despite this limitation, sampling frequency can be increased beyond the maximum analog bandwidth so that the 3dB cut-off frequency will naturally filter away the undesired harmonics. The minimum sampling frequency for the future observation

should be equal or higher than 200 kHz because for the Nyquist sampling theorem it is about the double of the analog bandwidth.

A first measure, that can corroborate future observation, is an input noise acquisition with a reference resistance of 50Ω . The instrument, terminated with an impedance of 50Ω acquires 200 ksamples with the sampling frequency of 200 kHz. Complete condition of measure are showed in the table 4.2.

bits number (Nbits)	24
sample frequency (f_s)	200 kHz
Number of samples (N)	20 M
Number of samples in a Window (W)	200000
Full scale range (FSR)	± 300 mV

Table 4.2: Default condition of measures

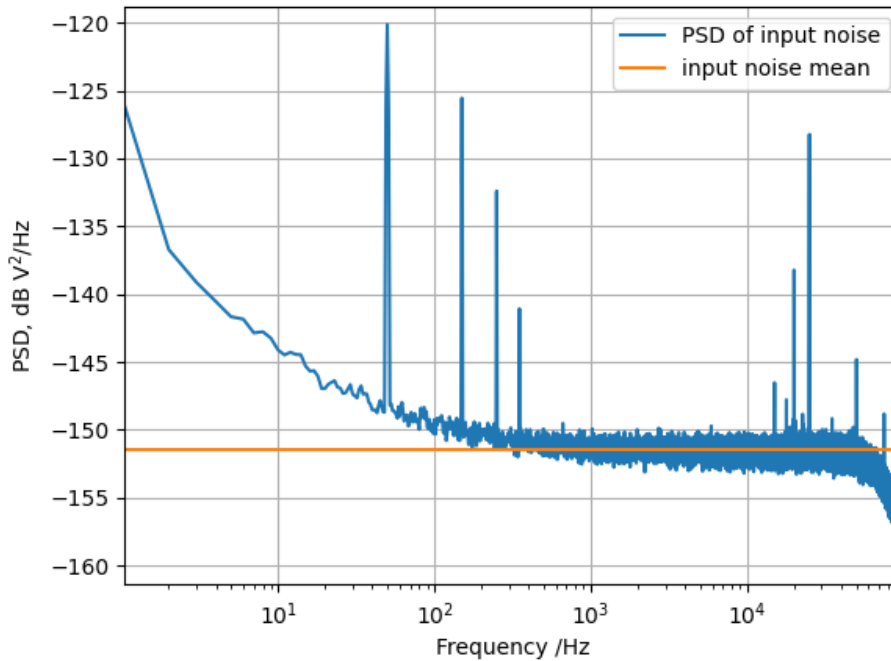


Figure 4.5: 50Ω termination measure (blue line), noise mean was performed between $[10^3 - 10^4]$ Hz (orange line)

In the figure 4.5 is depicted the PSD (Power spectral density, Appendix A.1) of the acquired samples when the termination is connected (Blue curve). Input noise

shows AC line noise at a frequency of 50 Hz and its multiples. The following calculation allows the theoretical estimation of quantization noise starting from the formula of SNR (Signal Noise Ratio).

$$SNR_{DAC} = 6.02 \cdot N_{\text{bits}} \text{ dB} + 1.76 \text{ dB} = 146.2 \text{ dB} \quad (4.1)$$

$$\text{Quantization Noise}_{\text{dB}} = \text{Signal}_{\text{dB}} - SNR_{DAC} \quad (4.2)$$

The "Signal" factor that is included in the SNR calculation is the Full-scale value, in this particular case the selected input range is ± 300 mV which means that a sine wave with 600 mV peak-to-peak can be applied to the input. Therefore RMS of the incoming signal is $\frac{0.3}{\sqrt{2}}$ V. The "Quantization Noise" factor is the theoretical minimum noise floor reachable by technology.

$$\text{Quantization Noise}_{\text{dB}} = -146.2 \text{ dB} + 10 \cdot \log_{10} \left(\frac{0.3^2}{2} \right) = -159.7 \text{ dB} = 14.6 \text{ nV} \quad (4.3)$$

The PSD of the theoretical quantization noise is its normalized version in the half of the sampling frequency

$$PSD_{\text{Quantization Noise}} = \text{Quantization Noise}_{\text{dB}} - 10 \cdot \log_{10} \left(\frac{f_s}{2} \right) \quad (4.4)$$

So the theoretical PSD of the quantization noise can be finally computed:

$$PSD_{\text{Quantization Noise}} = -159.7 - 10 \cdot \log_{10} \left(\frac{200 \text{ kHz}}{2} \right) = \quad (4.5)$$

$$-209.6 \text{ dB V}^2/\text{Hz} \quad (4.6)$$

In the figure 4.6 the mean value of the noise acquired by DAQ is compared with the theoretical Noise floor .

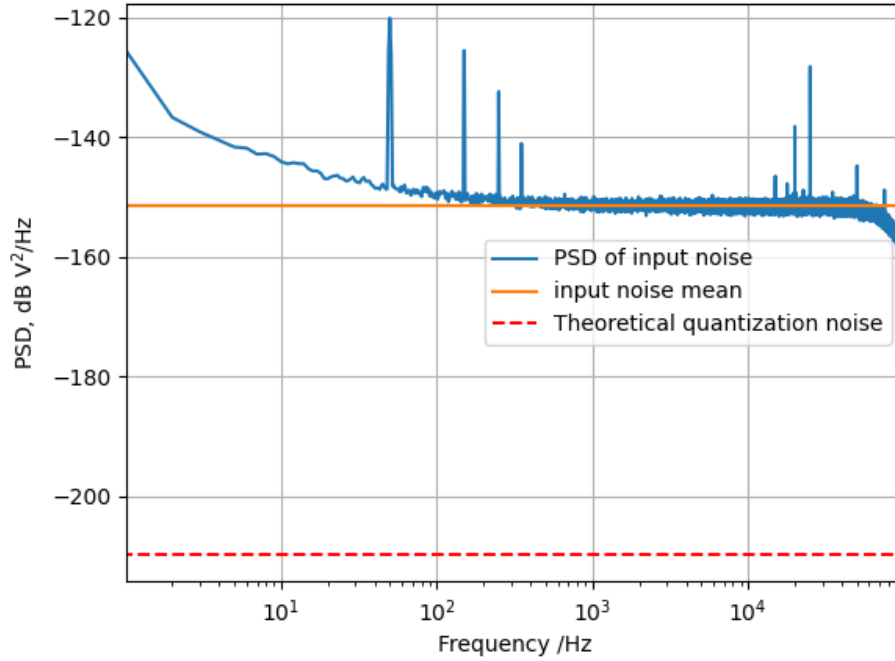


Figure 4.6: 50 Ω Noise vs Theoretical quantization noise. The theoretical value of the quantization noise in red dashed line ($-209.6 \text{ dB V}^2/\text{Hz}$) compared with the input noise in orange line ($-152 \text{ dB V}^2/\text{Hz}$)

Starting from the mean of the PSD of the detected noise (fig. 4.6, orange line) it is possible to compute the maximum SNR of the signal.

$$SNR_{MAX} = \text{PSD}_{\text{noise floor}} + 10 \cdot \log_{10} \left(\frac{200 \text{ kHz}}{2} \right) - 10 \cdot \log_{10} \left(\frac{0.3^2}{2} \right) = 88 \text{ dB} \quad (4.7)$$

Using as input the maximum SNR the ENOB (Effective Number Of Bits) is calculated as follows:

$$ENOB = \frac{SNR_{MAX} - 1.76}{6.02} \approx 15 \text{ bits} \quad (4.8)$$

The instrument presents a huge discrepancy between effective number of bits and the declared one.

4.2 DFB (Distributed Feedback) Laser Diode

The laser diode is the key component of this optical system and for this reason there are some features to be met. The first characteristic is related to the linewidth which is desired to be narrow to maximize pumping efficiency and frequency resolution useful for absorption measures. DFB (Distributed Feedback) Lasers are solid state photonic devices mostly used because of the presence Bragg grating in the active area of the device which allows laser cavity to resonate at a specific modal frequency. This category of emitter has a strong sidemode suppression ratio and a small linewidth. The Eagleyard Company manufactures DFB Tunable 780 nm Lasers it is particularly suitable for spectroscopy and has temperature control capability. Lasers of this typology are generally 8 pins models which is typical for devices controlled by TECs (temperature control devices).



Figure 4.7: EYP-DFB Eagleyard Photonics Distributed Feedback Laser

TEC performs tuning by observing temperature of a Thermistor (NTC, negative temperature coefficient) and cooling back with a Thermoelectric Cooler. This closed loop increases the laser frequency stability. A summary of laser characteristic are reported in the table 4.3.

linewidth	2 MHz
Center wavelength	779-781 nm
Output power	20 - 80 mW
Threshold Current	70 mA

Table 4.3: Eagleyard EYP-DFB Laser characteristics

4.3 Photodiode

Photodiodes are essential components in optical detection systems, converting incident light into an electrical signal through the photoelectric effect. Their high sensitivity, fast response time, and low noise make them particularly suitable for precision optical measurements. In this experiment, photodiodes were employed to measure the absorption of a 750 nm laser interacting with rubidium atoms. The chosen wavelength corresponds to a key transition in rubidium’s atomic spectrum, making accurate optical power detection crucial for analyzing the interaction.

Two different types of silicon photodiodes were used and analyzed:

- *Single photodiode*: Measures the laser intensity directly and is useful for basic power detection.
- *Balanced photodiode*: Composed of two matched photodiodes in a differential configuration, allowing for common-mode noise suppression and improved signal-to-noise ratio. This is particularly advantageous when dealing with fluctuations in laser intensity or environmental noise.

4.3.1 Single Photodiode

Thorlabs PDA36A2 is a Silicon switchable gain photodiode (fig. 4.8a). The chosen model has a working wavelength range that covers the interval 400-1100 nm compliant to the wavelength of the laser ($\lambda=780$ nm).

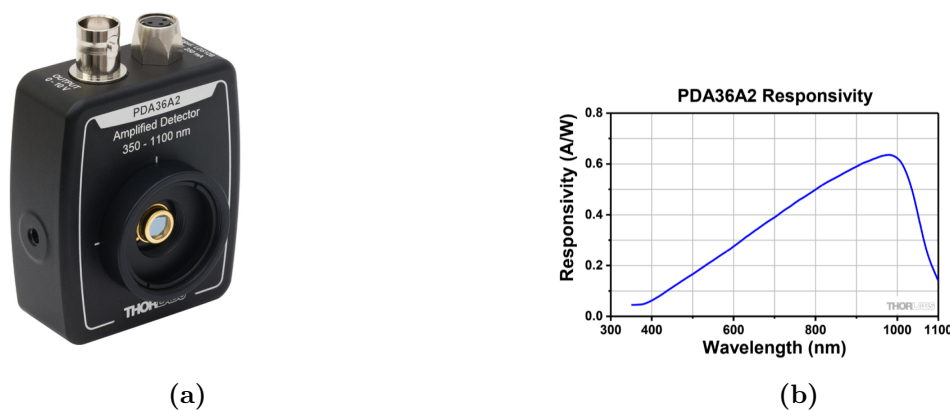


Figure 4.8: Thorlabs PDA36A2 Si Switchable Gain Detector: (a) Physical package, (b) Responsivity, taken from [33]

The table 4.4 shows the main features of the photodiode and some useful information about the interface of the detector in order to connect it inside the complete system.

Gain values	0 - 70 dB (10 dB step)
Output impedance	50 Ω
Output Range	0 - 10 V
Active Area	3.6 mm x 3.6 mm (13 mm ²)

Table 4.4: Thorlabs PDA36A2 Photodiode features

The so called scaling factor (SF) is caused by the voltage divider formed by the diode output impedance (R_S) and the DAQ input impedance (R_{Load}). The voltage divider is the following:

$$SF = \frac{R_{load}}{R_{load} + R_S} \quad (4.9)$$

By imposing R_{Load} equal to 1 M Ω and R_S equal to 50 Ω , the total *scaling factor* is 0,99. Observing the picture 4.8b, taken from the photodiode's datasheet it's possible to compute the responsivity by selecting the proper wavelength. By the means of a curve fitter (python tool) the value of responsivity = 0.47 A/W was found fixing $\lambda = 780$ nm. The formula that describes how output voltage is linked to photodiode characteristics is displayed below (eqn. 4.10) linking the photodiode responsivity ($R(\lambda)$, lambda dependent) with the transimpedance gain (G) (possible gain is showed in the tab. 4.4), the scaling factor and the input power (P_{in}).

$$V_{out} = R(\lambda) \cdot G \cdot SF \cdot P_{in} \quad (4.10)$$

The picture below (figure 4.9) represents a plot of the so called dark noise of the photodiode when no lasering power shines on it. A preliminary consideration about the spikes in the figure reveals two interference phenomena: laboratory neon lights interferes with the detection; 50 Hz power supply frequency and its sub-carriers are responsible for the internal operational amplifiers distortions.

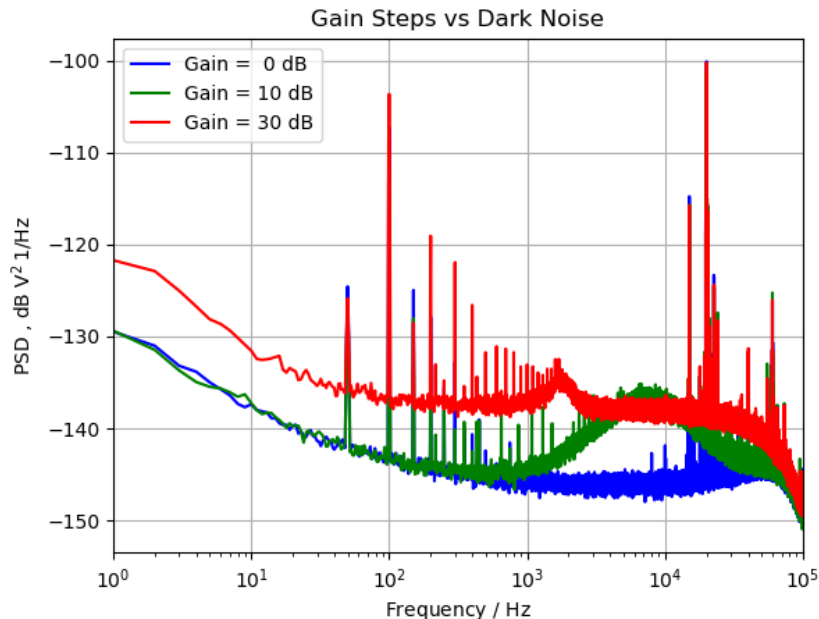


Figure 4.9: Dark noise of a single photodiode with variable gain 0 dB (blue curve), 10 dB (green curve), 30 dB (red curve).

The choice of a photodiode gain equal to 30 dB is related to the maximization of the input range which means that for weaker lasering power gain is higher. Another good motivation that influences this decision is the higher SNR reachable (in the measurement chain) with an increased gain.

4.3.2 Balanced Photodiode

Balanced photodiodes are a specialized type of photodiode that integrate an operational amplifier circuit within them. These devices are particularly useful when attenuation of common-mode noise is required. They consist of a differential amplification system with two silicon photodiodes. The specific model used, the Thorlabs PDB250A, ensures a common-mode noise reduction of more than 35 dB.

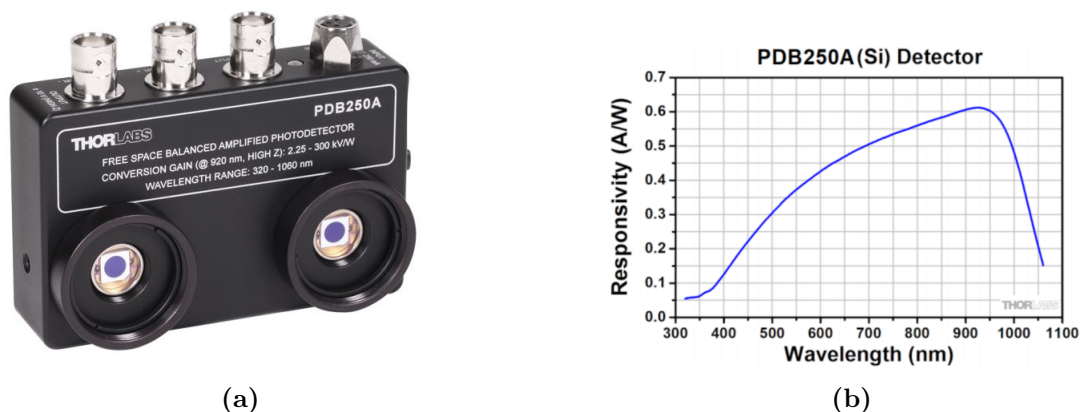


Figure 4.10: Thorlabs PDB250A Si Switchable Gain Balanced Detector: (a) Physical package , (b) Responsivity, taken from [34].

The responsivity plot of the differential photodiode is shown in Figure 4.10b. The plot indicates that, at a fixed wavelength of $\lambda=780$ nm (laser wavelength), the responsivity reaches 0.55 A/W.

Output RF	
Output impedance	100 Ω
Bandwidth (3 dB)	DC to 1 MHz
Conversion Gain [min – max]	$2.25 \cdot 10^3$ - $300 \cdot 10^3$ V/W
Output Monitor	
Output impedance	200 Ω
Bandwidth (3 dB)	DC to 10 kHz
Conversion Gain	$10 \cdot 10^3$ V/W

Table 4.5: Thorlabs PDB250A Photodiode features.

Like observed in the picture 4.10a this device present three outputs: one called RF port and two Monitor probes. Monitor outputs has a fixed conversion gain (tab. 4.5) independent from the gain lateral knob, in fact this is channel was used only to monitor the incident power. RF output presents a larger bandwidth and a variable conversion gain. The RF port is the output of a transimpedance amplifier, 8 variable steps are used to modify its conversion gain (G_{RF}). It can reach, observing the table 4.5, the value of $300 \cdot 10^3$ V/W. Voltage of the RF channel is expressed by the following equation:

$$V_{RF} = (P_{M+} - P_{M-}) \cdot R(\lambda) \cdot G_{RF} \quad (4.11)$$

The monitor power contributions offered by the two channels (P_{M+} and P_{M-}) are subtracted and multiplied by the usual resistivity factor $R(\lambda)$ and G_{RF} , the RF conversion gain selected by user.

The voltage equation for a single monitor channel is given by equation 4.12, where the monitor's conversion gain differs from that of the RF channel.

$$V_{M+} = P_{M+} \cdot R(\lambda) \cdot G_M \quad (4.12)$$

Differential photodiodes are used when it is necessary to suppress common mode noise contributions on two distinct laser path in order to isolate component of noise not correlated between them. Recalling the RIN definition and its link with the α (fluctuation of the signal) factor:

$$\begin{aligned} P &= \langle P \rangle (1 + \alpha) \\ RIN &= S_\alpha \end{aligned} \quad (4.13)$$

Using the values collected by RF and Monitor ports, α can be computed as follows.

$$\alpha = \frac{(P_{M+} - P_{M-})}{\sqrt{2} \langle P_{M+} \rangle} = \frac{V_{RF}}{\sqrt{2} V_{M+}} \frac{G_M}{G_{RF}} \quad (4.14)$$

The term $\sqrt{2}$ is used to normalize the α factor, assuming that P_{M+} and P_{M-} are uncorrelated. This assumption is justified by the fact that, in a differential measurement, the power spectral density of uncorrelated contributions doubles.

The selected gain step in order to guarantee a better resolution for the fixed input range is the gain step 8. This consideration is a direct consequence of the collected data of dark noise at different gain steps of the detector. "Dark noise" refers to the noise generated by the photodetector when no laser power is incident on it. In particular, figure 4.11 presents RIN_{RF} with the highest gain as possible and the minimum one showing that maximum gain means also a lower RIN_{RF} spectrum. It is possible to represent a view of the minimum RIN that the RF output can reach with a variable normalization factor.

Figure 4.12 shows how the hypothetical input power variation affects the RIN level, revealing that higher power leads to a lower RIN.

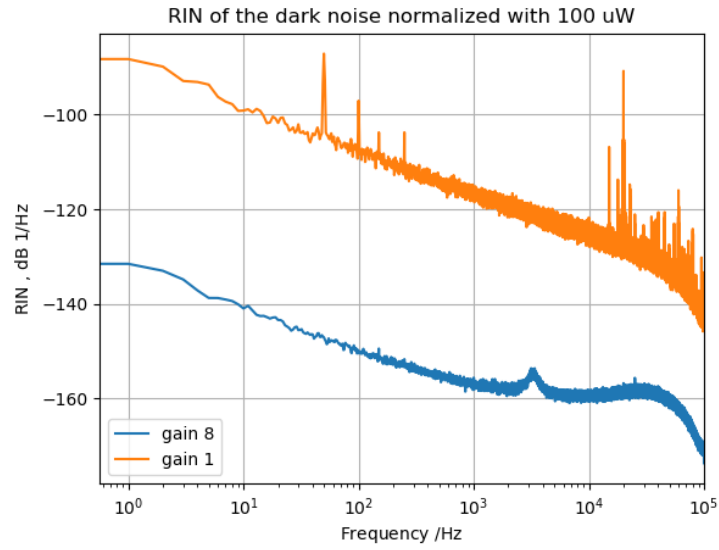


Figure 4.11: Measured differential Gain steps vs the RIN of the RF channel following the definition of 4.14 with no input power. The RIN is performed assuming a monitor power of $100 \mu\text{W}$

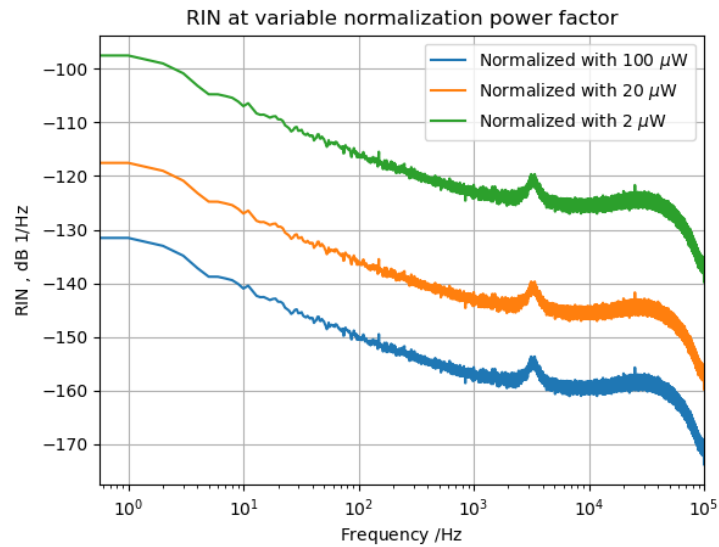


Figure 4.12: RIN of the dark noise with varying normalization power levels ($100 \mu\text{W}$, $20 \mu\text{W}$, $2 \mu\text{W}$)

Chapter 5

Measurement Technique for Relative Intensity Noise

This chapter focuses on determining the main noise contributions of the laser to assess the proper functioning of the measurement system. The analyzed setup consists of photodiodes, a data acquisition board, and local signal processing program written in python language. All information about the code are reported in the appendix A.

- In *Section* 5.1, the shot noise of the laser is analyzed using a balanced photodiode. This configuration inherently removes common-mode noise, isolating the fundamental shot noise limit of the laser. By comparing the measured noise with theoretical predictions, it is possible to confirm whether the system is operating as expected.
- In *Section* 5.2, the Relative Intensity Noise (RIN) of the laser is evaluated using two single photodiodes. The method is based on the cross-correlation of the signals acquired from two independent detectors, allowing the extraction of the laser's intrinsic noise while minimizing uncorrelated contributions.

The results obtained in both sections provide a comprehensive evaluation of the system's performance, ensuring that the measurement setup is reliable and it can be expanded in order to detect other kinds of noise contribution.

5.1 Laser Shot Noise Measurement with Balanced Acquisition

Differential measures are usually used to increase the resolution of a measure suppressing a common mode noise offered by a system. The following test bench is used to quantify the laser shot noise employing a balanced photodiode thus in the RF output laser technical noise is subtracted.

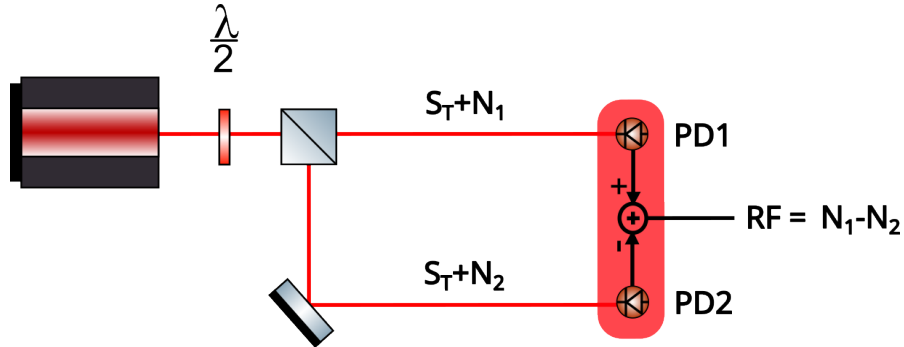


Figure 5.1: Simplified double photodetector setup. In the scheme are presented a polarizing beam splitter, a mirror and a balanced Thorlabs photodiode (red box), see section 4.3.2.

The figure 5.1 is a very simple optical circuit with one laser source and a beam splitter which allows the light to be divided into two equal powered signals with orthogonal polarization. The beam splitter separates the s and p-polarization into two contributions reaching the two photodetectors connected to the DAQ. By performing a differential measurement, the common-mode noise is canceled out through signal subtraction, leaving only uncorrelated contributions in this case, the two shot noise components N_1 and N_2 .

The Laser power is detected with a power meter and the collected values are used to plot the expected shot-noise level. As observed in section 4.3.2, the RIN of the shot noise can be obtained by the RF Output thanks to the α (relative fluctuation) of the balanced photodiode normalized with the average input power ($\langle P \rangle$) of the monitor. The equation below represents this computation:

$$S_\alpha = \frac{N_1 - N_2}{2 \langle P \rangle^2} = \frac{2h\nu \langle P \rangle}{\langle P \rangle^2} = RIN_N \quad (5.1)$$

To verify this setup in practice, two different scenario are tested with two operative laser power conditions: $20 \mu\text{W}$ and $4.6 \mu\text{W}$.

First case is showed by the figure 5.2, a plot of the ideal shot noise (orange line) compared with the RF output (blue line) and the photodiode dark noise floor (green line). It is possible to observe that the ideal value is reached by the blue curve in the region [0.5 kHz - 10 kHz] where orange line and blue line are overlapped.

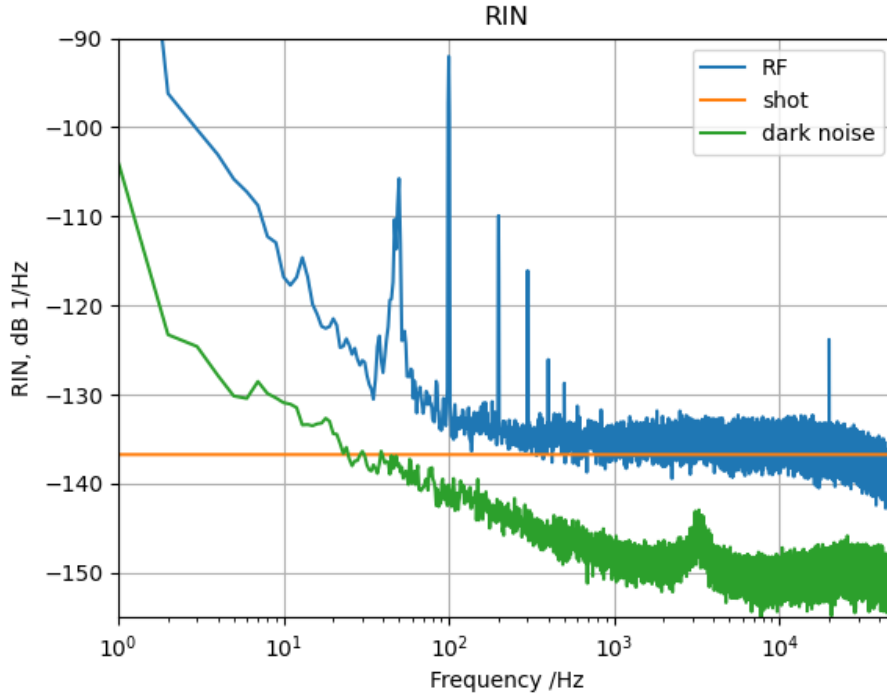


Figure 5.2: Double photodetector setup results, data are collected for a laser power of 20 uW. In the image: theoretical shot noise (orange curve), dark noise when laser power is not present (green curve) and the RIN_N of the differential measure.

In the second case (Figure 5.3) the average input power ($\langle P \rangle$) is lower which reflects an higher RIN shot noise. In addition to that, the electronic contribution in the second case, is closer to the input power value. The main consequence of this behavior is that the blue line has an higher mean value respect to the orange one in the reference range [0.5 kHz - 10 kHz].

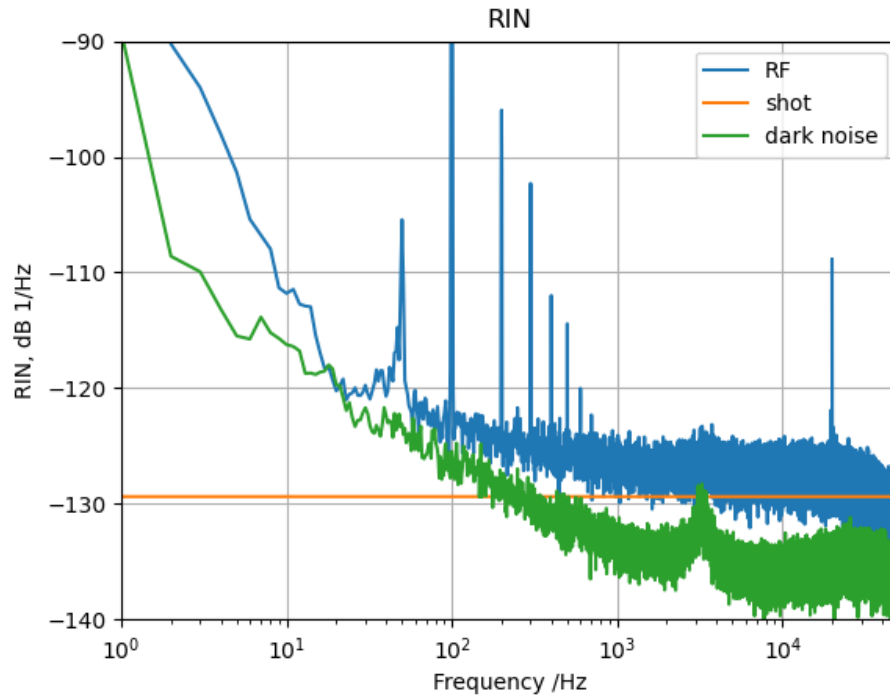


Figure 5.3: Double photodetector setup results, data are collected for a laser power of 4.6 μ W. In the image: theoretical shot noise (orange curve), dark noise when laser power is not present (green curve) and the RIN_N of the differential measure.

5.2 Laser Technical Noise

This section introduces a basic test of the cross-correlation block to validate its operating principle. Cross-correlation enables the measurement of laser technical noise, represented by the factor S_T , while isolating it from unwanted contributions such as shot noise N . When a laser beam is split by a beam splitter, both resulting beams are influenced by two types of noise: shot noise and technical noise. However, while shot noise remains uncorrelated between the two beams, the laser's technical noise is correlated. The block diagram in Figure 5.4 illustrates the acquisition setup. The recorded signals are processed using a Python script that applies cross-correlation functions (see appendix A).

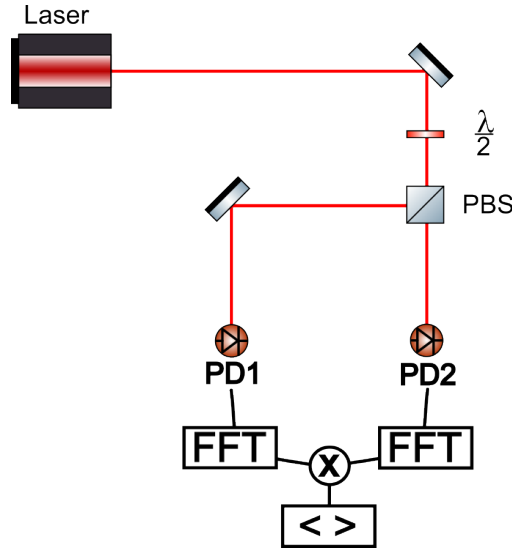


Figure 5.4: Simplified RIN measurement optical setup (PD1 and PD2 are two photodiodes while PBS a polarizing beam splitter).

Equation 5.2 expresses the relationship between the cross-spectrum of the channels and the laser's Relative Intensity Noise (RIN).

$$RIN_L = \text{CSD}\left(\frac{P_{D1}}{\langle P_{D1} \rangle}, \frac{P_{D2}}{\langle P_{D2} \rangle}\right) = \frac{S_T(f)}{\langle P \rangle^2} \quad (5.2)$$

Following plots proves the independence between the RIN of the laser noise and the power in three power scenario: $20 \mu W$, $160 \mu W$, $470 \mu W$. The green curves, representing the real part of the cross-correlation, has the expected trend of the RIN which decreases with the law f^{-1} . The f^{-1} dashed fitting green curve is always the same in every situation proposed totally independent from input laser power.

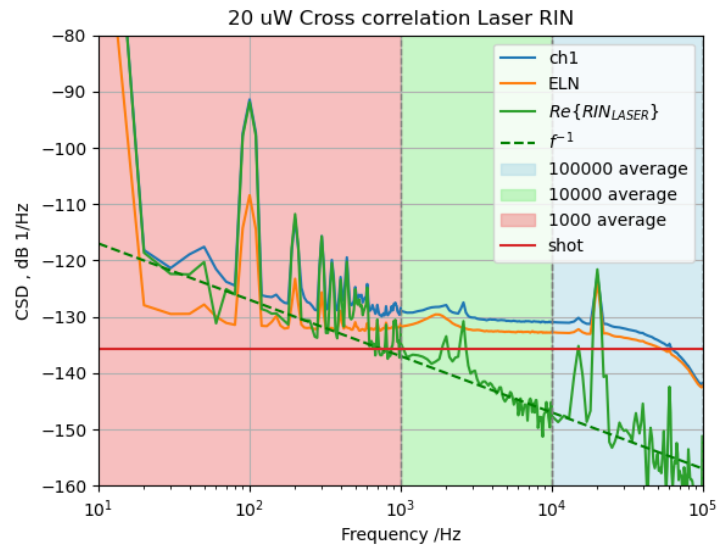


Figure 5.5: Technical noise setup results fixing the input power detected by photodiodes at $20 \mu W$.

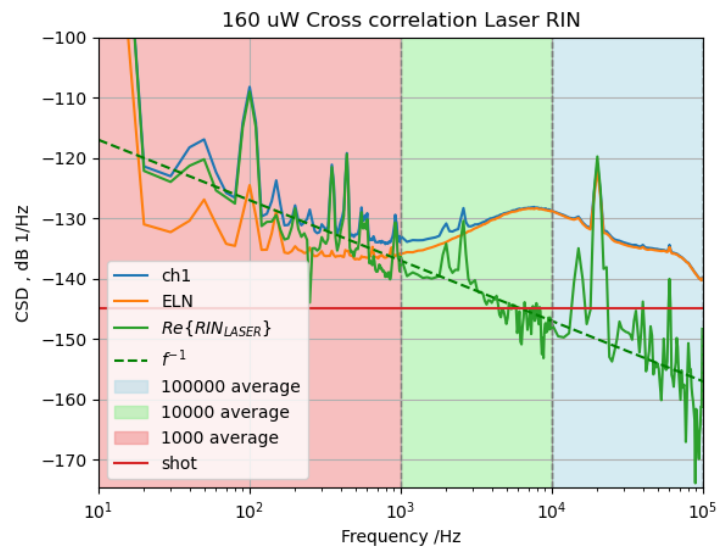


Figure 5.6: Technical noise setup results fixing the input power detected by photodiodes at $160 \mu W$.

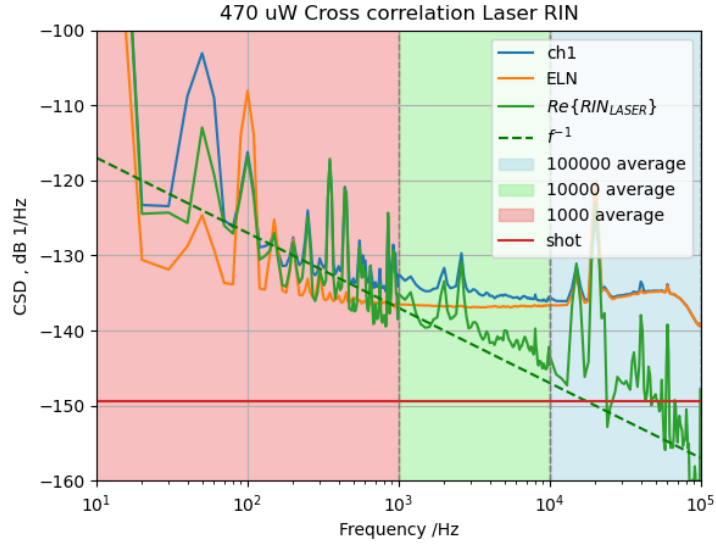


Figure 5.7: Technical noise setup results fixing the input power detected by photodiodes at $470 \mu W$.

Like showed in figure 5.5 the case with input power of $20 \mu W$ is the case with the highest shot noise. Three power case scenarios confirmed expectations on the RIN technical noise which presents the expected slope f^{-1} as seen in the chapter 2. The plots shown in this section, as explained in section 3.3, is a representation of the real part of XY^* as the best estimator of the cross-spectrum. In order to improve the number of averages, a method that treats the high and low-frequency part of the spectrum differently is implemented: for computing the high-frequency FFT, shorter averaging windows were chosen, increasing the number of averages at the cost of lower spectral resolution. the number of averages for each decade are shown with different background colors in Fig.5.5 - 5.7. More details on the data analysis can be found in appendix A.3. As evident from the comparison with the PSD obtained with the single photodiodes (blue curves) and with the theoretical shot noise levels (red curves), the cross-correlation method allowed us to measure the laser RIN at levels below these unwanted noise sources. This is especially true at high Fourier frequencies, were the laser diode RIN is lowest.

Chapter 6

Measurement Technique for Atomic noise

This chapter contains the description of the technique used to measure the Brownian atomic noise using the experimental setup (see figure 3.9) described in chapter 3. The measurement of the relative intensity noise due to the atomic motion has been taken with the laser resonant with the D2 atomic line, at different detunings from the atomic resonance. In Section 6.1, a brief introduction of the atomic absorption spectra is given, in order to better contextualize the experimental conditions at which the noise measurements were performed.

The spectra of a reference cell, with pure rubidium, was used as laser frequency calibration, this phase is described in Section 6.2; it allows an easy positioning along rubidium absorption curve. Thanks to this calibration process it is possible to relate the measured atomic noise with laser detuning.

The final experimental setup and a discussion of the most promising results are presented in Section 6.4.

6.1 Introduction on Atomic Absorption

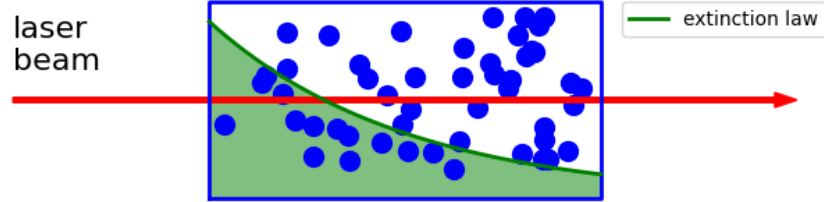


Figure 6.1: Figurative description of the extinction law 6.2 with a laser (red arrow) crossing an atomic medium (blue dots).

When a laser beam propagates through a diluted atomic sample its attenuation in intensity, I , is described by the differential equation 6.1. The attenuation coefficient k depends on the laser tuning frequency ω_L .

$$\frac{dI}{dz} = -k(\omega_L)I \quad (6.1)$$

Assuming that the beam propagates along the z -axis, like showed in the figure 6.1, the solution of the previews equation 6.1 is the following extinction law [13], an exponential decreasing trend along the propagation axis called Lambert-Beer equation:

$$I(\omega_L, z) = I(\omega_L, 0)e^{-k(\omega_L)z} \quad (6.2)$$

The same equation can be defined fixing a specific z value: the length of the cell inside which the atomic vapor is confined, L .

$$I(\omega_L, L) = I(\omega_L, 0)e^{-k(\omega_L)L} \quad (6.3)$$

Every orthogonal section of the cell can be seen as a parallelepiped with a thickness of Δz (fig. 6.2).

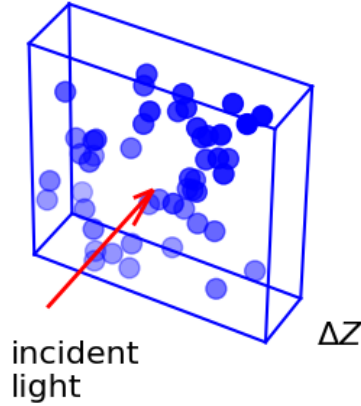


Figure 6.2: Δz vertical section of a cell containing an atomic medium (blue dots).

The differential equation is transformed into a finite difference relation 6.4; the coefficient k is proportional to n , the number of atoms per unit volume. The factor $n\sigma\Delta z$ is the fraction of the target area that is covered by the atoms (the "obstacle" that light encounters) where σ is the atomic cross-section.

$$\frac{\Delta I}{I} = -k\Delta z = -n\sigma\Delta z \quad (6.4)$$

One strategy to measure $k(\omega_L, L)$ indirectly is to measure the normalized power and apply the natural logarithm in order to resolve the exponential equation 6.3.

$$k(\omega_L, L)L = -\ln\left(\frac{I(\omega_L, L)}{I(\omega_L, 0)}\right) \quad (6.5)$$

This general formula will be used in the following sections to convert the exponential dependence between the intensity and the absorption coefficient.

6.1.1 Doppler Broadening

If the laser shine a vapor cell, every atoms perceive a different frequency due to their relative motion respect to the incident light. This Doppler effect is generated by each rubidium atom because they have different directions and speed inside the cell.

$$\omega'_L = \omega_L - \vec{k} \cdot \vec{v} \quad (6.6)$$

The shifted frequency ω'_L (eq. 6.6) is composed by the laser frequency ω_L subtracted with the scalar product between the atomic velocity \vec{v} and \vec{k} , the wave-vector which

propagates orthogonal with a magnitude of ω_L/c . The Boltzmann distribution (equation 6.7) is used to describe how velocity is distributed

$$f(v) = \sqrt{\frac{M}{2\pi K_B T}} e^{-\frac{Mv^2}{2K_B T}} = \frac{1}{\sqrt{\pi}u} e^{-\frac{v^2}{u^2}} \quad (6.7)$$

This equation depends on the atomic mass M , Boltzmann constant k_B , temperature T . The standard deviation of the Gaussian distribution of velocity is u which multiplied with the magnitude of k retrieves the standard deviation σ_D of the Gaussian that represents atomic absorption.

$$\sigma_D = \sqrt{\frac{2\pi K_B T}{Mc^2}} \omega_{12} \quad (6.8)$$

Doppler effect creates a broadening for every hyperfine level creating a Gaussian absorption profile with the parameter σ_D [13].

6.2 Calibration: Rb cell saturated absorption spectroscopy

This section describe how the calibration procedure was guided starting from tracing the absorption profile of the reference cell, with pure rubidium which was used as a frequency marker. Results of this section strongly rely on equations described in sections 6.1 and 6.1.1. The figure 6.3 represents the calibration setup, it is possible to observe both cells: reference cell with pure ^{87}Rb used for calibration and the cell used for future measurements with ^{87}Rb diluted in buffer gas.

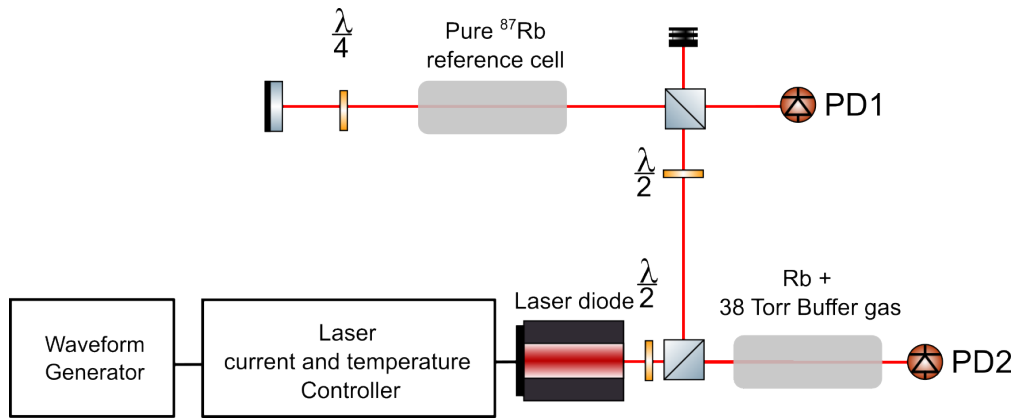


Figure 6.3: Block diagram representation of measurement circuit used for absorption profile

In order to describe calibration phase is necessary to introduce the Saturated absorption spectroscopy, an highly sensitive technique used to measure the absorption properties of atoms or molecules. It avoids the broadening effects caused by Doppler shifts thanks to two counter-propagating laser beams. The laser is tuned close to the rubidium transition $5S_{1/2} \rightarrow 5P_{3/2}$, so that, the reference cell, which contains pure rubidium atoms is shone with the light source twice by means of a mirror. The second reflected beam is orthogonal polarized thanks to a $\lambda/4$ filter which, due to its position, crossed twice, making possible the rotation in polarization. These two distinct laser rays defined as **Pump** and **Probe** allow the detection of energy levels in the absorption profile normally obfuscated by the Doppler broadening effect. The pump beam is responsible for creating a population imbalance in resonant atoms, while the counter-propagating wave detects the excited atoms. When beams interact with atoms that have almost zero velocity, $v_z = 0$ (the component of velocity parallel with beams) probing results in a "dip" in the final absorption spectrum. This phenomenon is called **hole burning**.

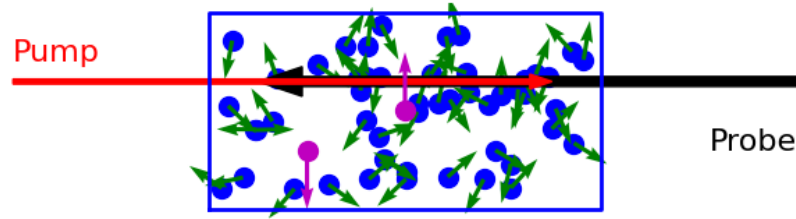


Figure 6.4: Rubidium atoms (blue dots) and their velocity (green vectors), magenta vectors highlights the condition $v_z = 0$.

The group of atoms that creates the holes in the final absorption spectrum are showed in the figure 6.4. Their velocity vectors are orthogonal to the two counter-propagating beams (magenta atoms). The waveform generator in the figure 6.3 creates a triangular shape voltage sweep which controls the laser frequency. The waveform generator sweep is acquired also by the DAQ with the photodiode in order to synchronize the acquisition with a proper python script. In figure 6.5 the relative absorption profile of the rubidium is plotted, $K(f)L$.

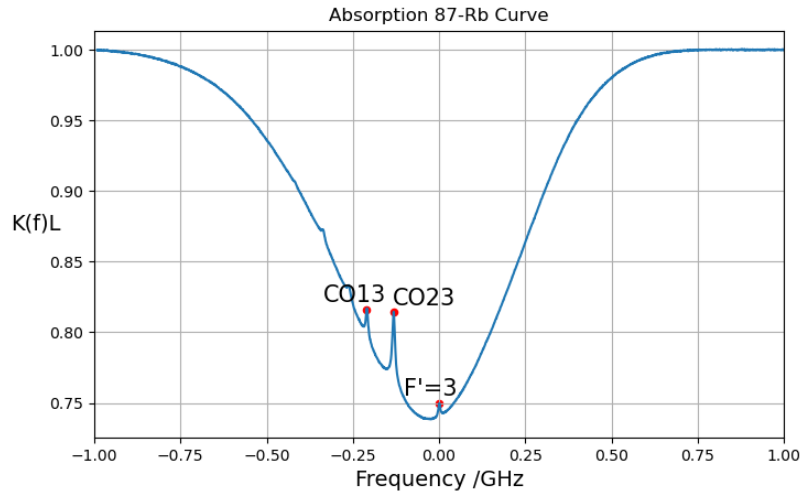


Figure 6.5: ^{87}Rb absorption spectrum red dots highlights the reference calibration "dips": cross-over CO13, CO23 and the energy level $F'=3$.

Observing the Doppler-resolved dips it is possible to observe dips where no resonance lines are present. These new peaks are called **cross-over** resonances, a phenomena that involves multi-level atoms like alkali metals. Observing a generic two energy level system with the hyper-fine structure $F'=1$ and $F'=2$ with $\omega_1 > \omega_2$ with the imposition of laser frequency to be $\omega_L = \frac{(\omega_1 + \omega_2)}{2}$. If a group of atoms present

$v_z = \frac{(\omega_1 + \omega_2)}{2} \frac{c}{\omega_L}$ an intermediate dip is created. For the multilevel case of the ^{87}Rb this phenomenon creates consistent dips for cross-over levels CO23, CO13, CO12 [35]. These new resonance levels are showed in the energy level image 6.6 with red dots.

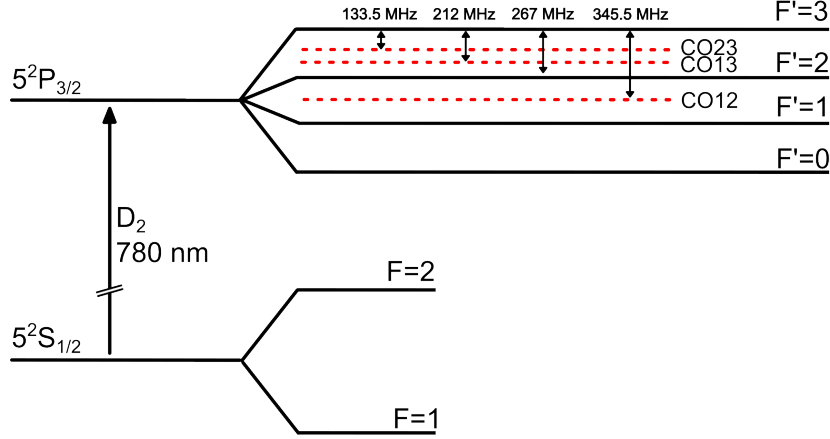


Figure 6.6: ^{87}Rb energy levels, cross-over levels are represented with red dashed lines.

The energy transition of interest for this analysis involves the ground level $F=2$ and the excited levels in the hyperfine structure and a first absorption model for this transition is the Gaussian one (eq. 6.9).

$$k(f) = -\frac{A}{\sigma} e^{-\frac{(f-f_0)^2}{2\sigma^2}} \quad (6.9)$$

The equation 6.9 is insufficient for the complete mathematical description of the phenomenon because there is a transition for every energy level of the hyperfine structure so that a Gaussian distribution associated to absorption. The admitted energy transitions starting from the ground level $F=2$ are the excited levels $F'=2, 3, 1$. The table 6.1 contains the frequency offset for each gaussian distribution and their relative strength factors C_F^2 (The maximum absorption rate for each level) that describes transition to the three hyperfine levels[36].

F'	offset frequency /MHz	C_F^2
1	0	1/18
2	156.95	5/18
3	423.59	7/9

Table 6.1: Strength factors and frequency offset for ^{87}Rb , taken from [36]

Formula 6.9 can be extended as follows:

$$k(f) = -\frac{A \cdot C1_F^2}{\sigma} e^{-\frac{(f-f_0)^2}{2\sigma^2}} - \frac{A \cdot C2_F^2}{\sigma} e^{-\frac{(f-(f_0+f_1))^2}{2\sigma^2}} - \frac{A \cdot C3_F^2}{\sigma} e^{-\frac{(f-(f_0+f_2))^2}{2\sigma^2}} \quad (6.10)$$

Using the formula 6.10 as a fitting equation a plot is traced (fig. 6.7) in order to compare the model and the actual observations.

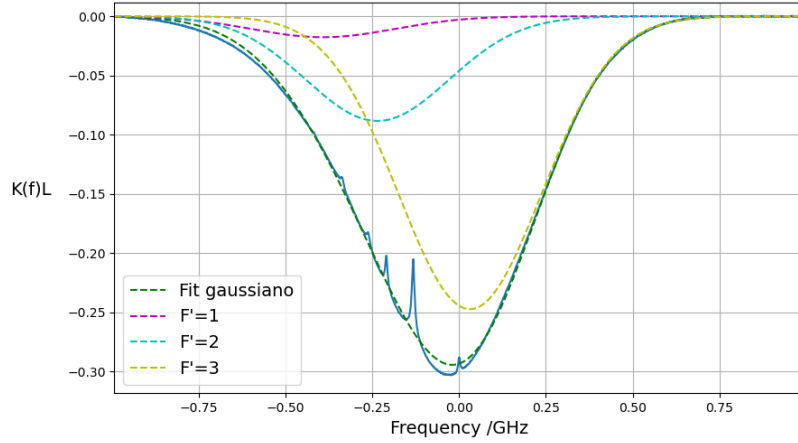


Figure 6.7: ^{87}Rb absorption spectrum with triple gaussian fit; dashed lines highlights: the complete absorption curve of the formula 6.10 (green curve), $F'=1$ gaussian (magenta), $F'=2$ gaussian (cyan), $F'=3$ gaussian (yellow).

Post-fitting parameters are extracted and showed in the box below.

A	0.065
f_0 /MHz	-392
σ /MHz	206

Table 6.2: Fitting results of the triple Gaussian fit

Confronting the experimental result with the theoretical one is possible to observe that the sigma σ_D (eq. 6.8) caused by doppler effect ($\sigma_D = \sqrt{\frac{k_B T}{M c^2}} \omega_L = 2\pi \times 215$ MHz) is closer to the observed sigma ($\times 206$ MHz).

6.3 Absorption Profile of the Rubidium Cell with Buffer Gas

Section 6.2 describes the process of laser tuning and relies on the cross-over dips of a pure rubidium cell fixing a voltage swipe with the signal generator. The absorption profile of a cell with buffer gas has no cross-over dips which highlights the importance the calibration setup 6.3.

After the determination of laser frequency range the buffer gas absorption measure can take place. To accurately measure atomic absorption the lineshape function is constructed by acquiring discrete DC measurements at fixed frequency points. Starting from this fitted resulting profile like shown in figure 6.8 the two collected profile can be compared on the common frequency axis.

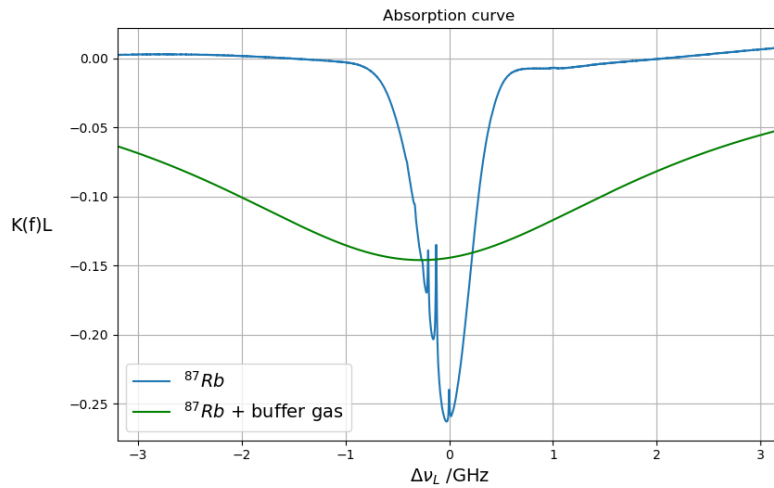


Figure 6.8: Calibration figure: reference frequency based on the pure rubidium absorption profile (Blue curve); the DC absorption profile of the cell diluted in buffer gas (Green curve).

The green curve represents the absorption profile of the broadened buffer gas cell and it is always measured overlapping a reference rubidium saturated absorption spectrum for comparison, blue curve, which is measured with the same modulation parameters for frequency axis reference. Buffer gas is a common solution to avoid wall collision, it creates a broadening effect in the final absorption curve that is summed up with the simple Doppler broadening. If Doppler effect implies a Gaussian profile the buffer gas contribution makes the profile a convolution between a Gaussian profile and a Lorentzian one [37] [38].

The equation 6.11 shows the definition of the Lorentzian profile.

$$L(\Gamma, A, f_0) = A \frac{(\Gamma/2)^2}{(f - f_0)^2 + (\Gamma/2)^2} \quad (6.11)$$

The parameter Γ describes the broadening of the absorption profile which is a fundamental information to understand the frequency range inside which atoms are resonant. After a fitting of the absorption curve with the buffer gas (see appendix D for Python code) the Γ parameter was extracted, $\Gamma = 4.97$ GHz.

6.4 AM Noise Atom Interaction

This section presents the measurements of the atomic noise performed on the Rb cell under test, filled with Rb and a mixture of Nitrogen and Ar buffer gases. The measurement setup follows the scheme of Fig. 3.9. The selected optical scheme used for characterizing atomic spectrum (see fig 6.9a) is composed by two laser beams that illuminate the rubidium cell, where they interact with the atomic medium. After exiting the cell, the beams are split by BS2 and BS3 that allow both paths to reach two balanced photodetectors. Photodetectors are responsible of common-mode suppression which makes possible thanks to the cross-spectrum between the signal RF1 and RF2 (photodetectors' outputs) to obtain the noise generated by the interaction between the two lasers and rubidium atoms, $S_A(f)$.

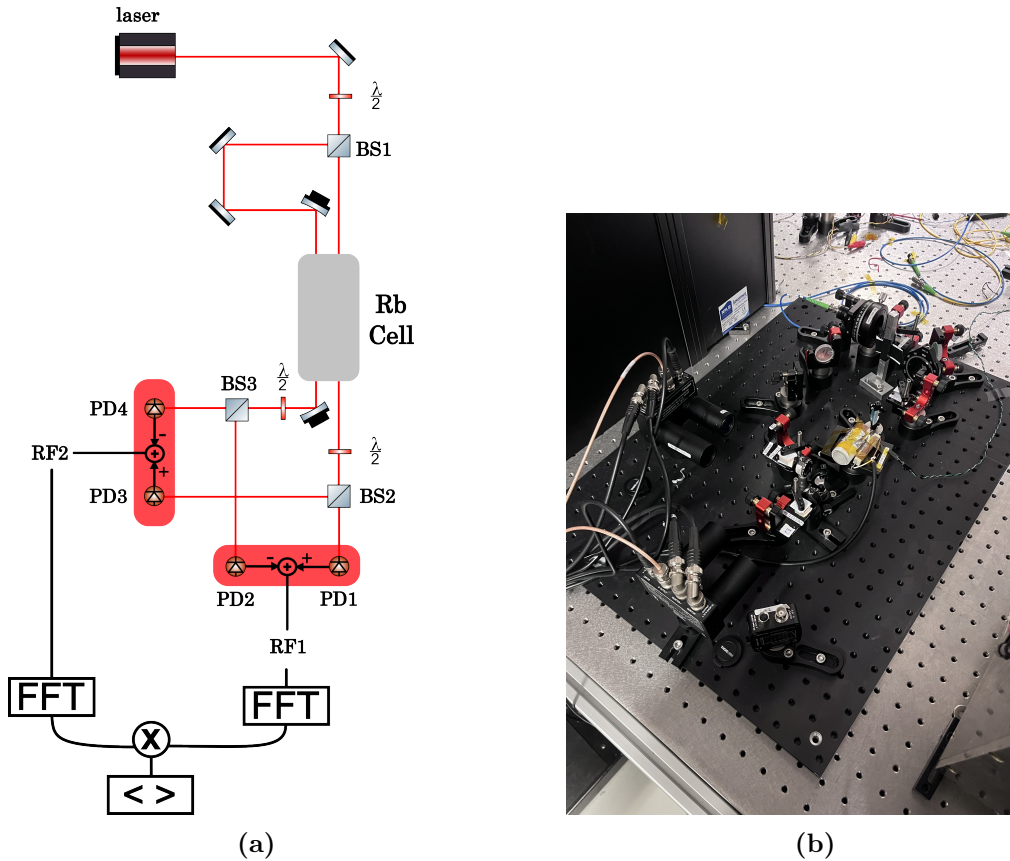


Figure 6.9: Final configuration: (a) Optical schematic of the acquisition setup, showing balanced photodiodes (highlighted in red), three beam splitters (BS1 - BS3) and a rubidium cell (gray box). (b) Physical implementation of the system.

Using the calibration procedure that allows the reconstruction of a DC absorption curve (section 6.3) it is possible to tune the laser to the center of the absorption profile. The figure 6.10 is the cross-spectrum in this particular tuning condition.

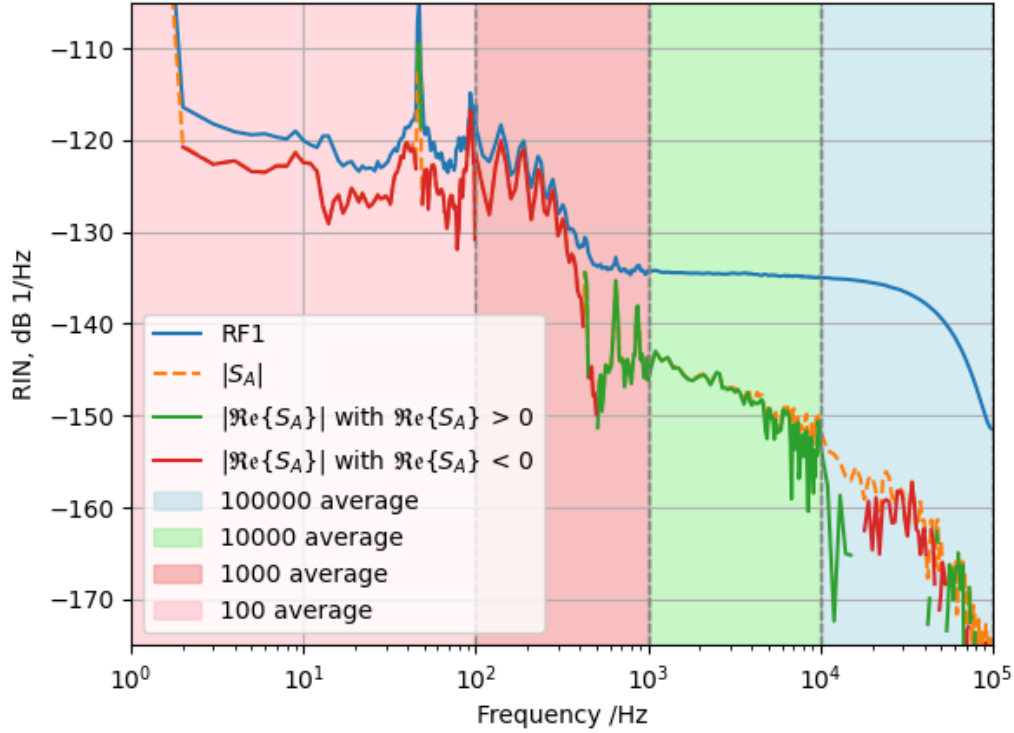


Figure 6.10: Figure shows the cross-correlation plot of the two differential photodiodes RF channels in correspondence of the maximum absorption coefficient, (Tuning the laser in the center of Lorentzian). The blue spectrum in the picture, the RF1 channel is compared with the two estimator or cross correlation $\Re\{S_A\}$ (green and red line) and $|S_A|$ (dashed orange line).

In the upper picture the two kinds of cross-correlation estimators are compared: $|S_A|$ and $\Re\{S_A\}$. Observing the magnitude of S_A (blue curve) in the low frequency range it presents some ripples multiples of the line frequency 50 Hz. In order to investigate deeply the reason of this spectrum profile the real part of S_A is splitted into its real and positive part (orange curve) and the negative one (green curve). In the low frequency range, the real part of the cross correlation is negative which suggest (like exposed in the chapter 3) that an anticorrelated contribution has an higher impact in this region. The spectral region, inside which the real part is positive, is concentrated in the range $[10^3 - 10^4]$ Hz.

In order to compute the high-frequency FFT (like showed in section 5.2) short averaging windows are chosen, increasing the number of possible averages (see appendix A.3). Moreover the performances of the measurement system are heavily sensible to the environmental neon light; mitigation of this effect was accomplished with a black plexiglass optical system cover.

Observations confirmed that the real part of the cross-spectrum for the region $[10^3 - 10^4]$ Hz is always positive independently from the laser tuning frequency. The measurement was then repeated at different detunings from the absorption profile minimum. In the figure 6.11, 5 points are selected on the absorption curve in order to use them as operative working points.

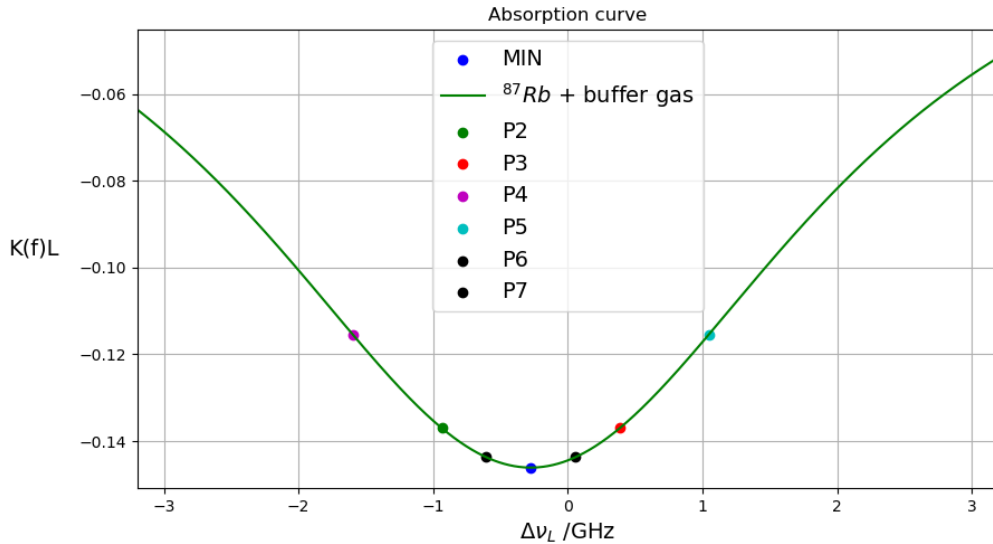


Figure 6.11: Colored points: MIN, P2, P3, P4, P5; they represent the operational points at which the intensity noise spectrum was measured.

For each tuning frequency across the absorption curve a spectrum of atomic noise was measured. Like observed previously the useful frequency range is $[10^3 - 10^4]$ Hz. The picture 6.12 represents cross spectrum in the condition of maximum absorption and in other two particular reference conditions: " 2Γ " (black curve) and "electronic noise" (magenta curve).

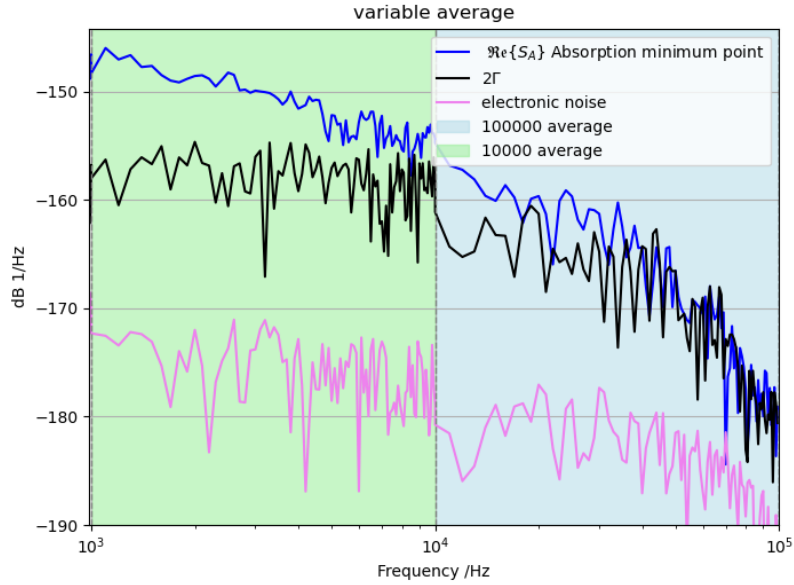


Figure 6.12: A zoomed portion of the cross-spectrum in the $[10^3 - 10^5]$ Hz spectrum range comparing the cross-spectrum measured in the maximum absorption point (blue curve) with the value obtained obscuring photodiodes (magenta line). The values of the cross-spectrum when the laser is tuned at 2Γ (black line).

First curve called " 2Γ " represents the response of the atomic medium at a frequency greater than 2Γ , where Γ denotes the frequency broadening of the Lorentzian absorption curve (see section 6.3). This operative condition was used to test the noise magnitude when the laser is tuned far from the center of the absorption curve. In this case, the laser was set to a detuning of -11.5 GHz, ensuring operation in a regime where absorption effects are significantly reduced.

The second "electronic noise" curve, is the spectrum of the cross-correlation in absence of illumination for both the balanced photodiodes. For this reason the "electronic noise" curve represents the noise contribution due to the measurement chain (differential photodiodes and data acquisition system).

In order to better visualize the dependence of the measured intensity noise with the laser detuning from the atomic resonance, we focused on the RIN value at a fixed Fourier frequency of interest. The choice of the frequency is limited in the range [1 kHz - 10 kHz], where the estimate of the cross-spectrum gave physically meaningful results.

The diagram, depicted in the figure 6.13, proves that the measured atomic noise is maximum when the absorption rate is the highest.

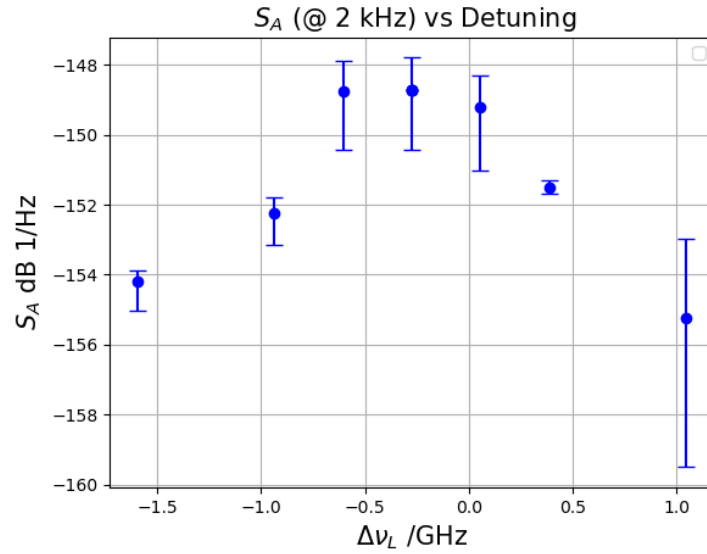


Figure 6.13: The image displays the magnitude of the measured atomic noise at a fixed Fourier frequency of 2 kHz. The x-axis represents the laser frequency, vertical bars are instead a visual representation of the uncertainty of the measurement.

Vertical bars are computed taking into account two main contribution of uncertainty which consists in: a type A contribution, given by the imaginary part of the cross-spectrum and a type B contribution, given by the accuracy of the DAQ. Statistical analyses presented in chapter 3 demonstrate that the imaginary part accounts only for uncorrelated noise sources. As the number of averages increases, this terms diminishes, as the CSD converges to the PSD of the correlated noise.

Chapter 7

Conclusions and Perspectives

This work demonstrated the effectiveness of the use of cross-correlation in noise isolation contribution. The first steps of the analysis involved the complete characterization of the instrumentation and optical components (chapter 4). Cross-correlation of two channels was performed first acquiring the laser technical noise (chapter 5) and only afterwards the atomic noise of a rubidium vapor-cell (chapter 6). The system used to measure the atomic noise of a rubidium vapor cell was ultimately composed of the following elements:

- **A differential acquisition schematic:** two signals which share a correlated noise contribution are splitted into two different path.
- **A fast data logger:** The acquisition device is responsible for the maximum bandwidth that is possible to acquire. Fast DAQ guarantees an higher bandwidth window.
- **Post-acquisition software:** A scripts which perform the cross-correlation of the acquired channel allowing the buried spectrum to emerges from the thermal noise floor.

Acquired data suggest that it is possible to measure a physical quantity even if it is corrupted by shot and electronic noises. This result highlights an important lesson: the usage of powerful and expensive instruments is not always a good choice to improve a measurement setup. Optimization can involve, in the digital era, post-acquisition algorithms which keep the total cost of the system unaltered and results more promising.

As a natural consequence of this work another experimental setup was tested facilitating the measurement of a different noise contribution which shares the same

detection difficulties of an low atomic noise. The same setup, presented in the previous chapters, was used to estimate the PM/AM conversion noise. A summary of this last experiment will be presented at the European Frequency and Time Forum (EFTF) [39].

The current observations represent an initial step for further research and provide a strong foundation for confirming new theoretical atomic models which are the basis for improving the performances of state-of-the art atomic clocks. The challenge presented by this experience was related to the limitations of the components used. New frontiers can be achieved by focusing on these two areas:

- **Hardware.** the usage of an instrument with an higher data-rate could increase performances and reduces the waiting time between subsequent acquisition. Higher data-rate means that fixing a certain time period more samples can be processed which means an higher number of averages.
- **Optical.** The substitution of inappropriate optical components can improve performances. In fact, PBS (polarizing beam splitter) could be substituted with non polarizing ones. Polarizing beam splitters separate incoming light into two orthogonal polarization components. If the input laser has polarization noise, it will affect the intensity noise of the two output beams. Furthermore, the two output beams will exhibit opposite intensity over time so that substitution of PBS prevents the formation of anti-correlated laser beams.

Appendix A

Python Spectrum Functions (`Spectra_lib.py`)

This appendix provides detailed information on the definition of each mathematical function used throughout this work. Each section is structured into two main parts: the theoretical background and its corresponding Python implementation. The theoretical part explains the mathematical principles and formulas behind each function, while the implementation part demonstrates how these functions are coded and utilized in Python. All the functions described in the following sections have been consolidated into a single, unified Python library called *Spectra_lib.py*, which is available on GitHub [40]. This library has been integrated into every processing script used for data acquisition, ensuring consistency and ease of use across the project.

A.1 PSD

The PSD (**Power Spectral Density**), usually described as the distribution of power across individual frequency components of a measured signal, is a mathematical tool strongly used in mechanical, electrical, and electronic systems as well as across numerous engineering disciplines. Harmonic analysis is a complete and exhaustive method in order to evaluate the Power distribution of a specific source of noise.

Definition

Given $x(t)$ a stochastic physical quantity and its time windowed version $x_T(t)$ such as:

$$x_T(t) = \begin{cases} x(t), & \text{if } |t| < T, \\ 0, & \text{if } |t| > T. \end{cases}$$

The PSD of $x(t)$ is

$$PSD_x(f) = \lim_{T \rightarrow \infty} \frac{\mathbb{E}[|X_T(f)|^2]}{2T}$$

The definition of an algorithm to estimate the Power Spectral Density has two main goals: Speed up the computation, display clear plots. There are two main methods of estimation:

1. **Bartlett's Method**, a general purpose Method
2. **Welch's Method**, an efficient variation of the Bartlett's Method

A.1.1 Bartlett's Method

Bartlett's Method consists in computing the DFT (Discrete fourier transform) several times over contiguous and non overlapping time windows. It is possible the FFT computation in the first window of M samples such as,

$$X_0(k) = \mathcal{F}\{x[0], x[1], x[2], \dots, x[M - 1]\} \quad (\text{A.1})$$

The second window will be,

$$X_2(k) = \mathcal{F}\{x[M], x[M + 1], x[M + 2], \dots, x[2M]\} \quad (\text{A.2})$$

If N time windows are available a number of N FFTs of distinct time portions can be obtained. The computation of the average of these FFTs is a good estimation of the PSD as follows

$$S_x(k) = \frac{1}{N} \sum_{j=0}^N |X_j(k)|^2 \quad (\text{A.3})$$

A.1.2 Welch's Method

Welch's Method is computed over 50 % overlapping windows instead of the consecutive and distinct time windows. The overlap mechanism is clearer in the following equations.

$$X_0(k) = \mathcal{F}\{x[0], x[1], x[2], \dots, x[M - 1]\} \quad (\text{A.4})$$

$$X_1(k) = \mathcal{F}\{x[M/2], x[1], x[2], \dots, x[3/2M - 1]\} \quad (\text{A.5})$$

$$X_2(k) = \mathcal{F}\{x[M], x[1], x[2], \dots, x[2M - 1]\} \quad (\text{A.6})$$

If the number of samples is fixed the Welch's Method has a double number of FFT which means that the equation that estimate PSD (A.7) will obtain a smoother trace.

$$S_x(k) = \frac{1}{N} \sum_{j=0}^N |X_j(k)|^2 \quad (\text{A.7})$$

This method is not a good choice if samples are acquired in different time slots with a conspicuous idle time between measures. In the case of a long pulse train of samples or short acquisition this method is perfect because it doubles the number of possible windows of the same input signal. By Fixing the duration of a generic data stream, chopped into m possible windows, the application of Welch method makes the number of windows equal to $2m-1$.

A.1.3 Python Code

The code below follows the mathematical notes already exposed. This minimum form can be considered a minimum form of the final algorithm, a small brick. `Psd_basic` has `x` as input value, `fs` as sampling frequency and finally `N` as number of samples. By looking in the box it's possible to observe computational constants in the final formula. Note that:

1. The PSD is divided by $N \cdot fs$ the resolution of the FFT because it is a density by definition
2. The PSD is multiplied by 2 because it is the right part of the spectrum and the total power must be always the same the 2 factor can compensate the lost contribution.

Psd_basic

```
import numpy as np
import scipy.fft as fft

def Psd_basic(x,fs,N):

    X = fft.fft(x) # fft of the input
    PSD = 2*(1/fs)*X*np.conj(X)/(N)
    freq = np.linspace(0,fs,N)

    return freq[0:int(N/2)], PSD[0:int(N/2)]
```

Two fundamental features are still missing to a proper PSD estimator:

1. **Windowing:** Without a windowing method the discontinuity at the boundaries of the acquired samples can not be mitigated.
2. **Averaging:** A good PSD estimator should include an averaging mechanism like shows the Welsh and the Bartlett's methods.

In order to solve the first problem the window generator functions (`windows.get_windows`) of the `scipy` library can be used as a mask for `x` samples. The window can be represented as a train of pulses with the following discrete summation:

$$W(n) = \sum_{j=0}^N w_j \times \delta(n - j) \quad (\text{A.8})$$

The S factor is defined as the summation of the coefficients of the previous discrete windowing function [41].

$$S = \sum_{j=0}^N w_j^2 \quad (\text{A.9})$$

The new generic definition of the PSD which is totally independent from the shape of the window is now complete:

$$PSD_x = \frac{2 \times |X|^2}{S \times f_s} \quad (\text{A.10})$$

Mathematical equations allows a new function definition:

Psd_windowed

```
import numpy as np
from scipy import signal
import scipy.fft as fft

def Psd_windowed(self,x,fs,N,window = 'hann'):

    win = signal.windows.get_window(window,N)
    X = fft.fft(x*win)
    PSD = 2*(1/fs)*X*np.conj(X)/((win* win).sum())
    freq = np.linspace(0,fs,N)

    return freq[0:int(N/2)], PSD[0:int(N/2)]
```

Previous operations create a good basis to write a complete usable function comprehensive of an averaging operation and windowing function.

Psd_bartlett

```
import numpy as np
import scipy.signal as signal
import scipy.fft as fft

def Psd_bartlett(x, fs, avg, window, N):

    #window generation
    win = signal.windows.get_window(window, N)

    if (len(x)/N >= avg):

        psd_buff = []

        for i in range(avg):

            X = fft.fft(x[i*N:i*N+N]*win)
            app = (2/fs)*X*np.conj(X)/((win*win).sum())
            psd_buff.append(app)
        buff = np.array(psd_buff)
        PSD = (np.sum(buff , axis=0)/avg)

    else:

        X = fft.fft(x)
        PSD = (2/fs)*X*np.conj(X)/((win*win).sum())
        freq = np.linspace(0, fs, N)

    return freq[0:int(N/2)], PSD[0:int(N/2)]
```

A.2 CSD

The CSD (**Cross-Spectral Density**) expand possibility unlocked by PSD, the concept of single channel power distribution is substituted with the research of a relationship between two signals. This "relationship" is commonly measured with the cross-correlation function $R_{yx}(t)$ which is an integral method to enhance common characteristic of two signals.

Definition

Given $x(t)$ and $y(t)$, two stochastic physical quantities, the CSD of $x(t)$ and $y(t)$ is

$$CSD_{yx}(f) = \lim_{T \rightarrow \infty} \frac{\mathbb{E}\{\mathcal{F}[R_{y,x}(t)]\}}{2T}$$

It is possible to prove an equivalence between the Fourier transform of the cross-correlation function $R_{yx}(t)$ and the product of the two signals $X(f)^*$ (conjugate) and $Y(f)$ in the frequency domain.

$$\mathcal{F}[R_{y,x}(t)] = X(f)^*Y(f) \quad (\text{A.11})$$

By observing this property of cross-correlation (eqn. A.11) the equation that link PSD and CSD is the following one:

$$PSD_x(f) = CSD_{yx}(f) \quad \text{if} \quad y(t) = x(t) \quad (\text{A.12})$$

A.2.1 Python Code

Like seen in the previous section new features are necessary in order to improve the functionality of the python library exploiting such as windowing and averaging. By following previous tips and definitions the implementation is really easy to understand.

Csd_basic

```
import numpy as np
import scipy.signal as signal
import scipy.fft as fourier

def Csd_basic(x, y, fs, avg, window, N):

    #window generation
    win = signal.windows.get_window(window, N)

    if (len(x)/N >= avg):

        csd_buff = []

        for i in range(avg):
```

```
        X = fourier.fft(x[i*N:i*N+N]*win)
        Y = fourier.fft(y[i*N:i*N+N]*win)
        app = (2/fs)*Y*np.conj(X)/((win*win).sum())
        csd_buff.append(app)

    buff = np.array(csd_buff)
    CSD = (np.sum(buff , axis=0)/avg)

else:

    X = fourier.fft(x)
    CSD = (2/fs)*X*np.conj(X)/((win*win).sum())
    freq = np.linspace(0,fs,N)

return freq[0:int(N/2)], CSD[0:int(N/2)]
```

Notice that CSD has an imaginary part and a real part ; PSD, instead, can reach only real values. The real part and an imaginary part of the cross-spectrum have two different meaning that should not be confused. The absolute value of CSD has a simpler and straight forward meaning as it is the measure of how much the two channel are correlated each other.

A.3 Advanced Averaging Methods

Observing logarithmic plots it is possible to notice that higher frequencies doesn't need the same resolution of the lowest one. It is possible to store a smaller amount of frequency points to observe similar quality of an higher resolution one. Resolution is linked to the windowing technique. Final resolution of a FFT plot will be the ratio between the sample frequency and the number of samples per windows. Assuming that the final spectrum plot will be divided into decades, higher decades can use smaller window instead lower decades uses the higher one (figure A.1).

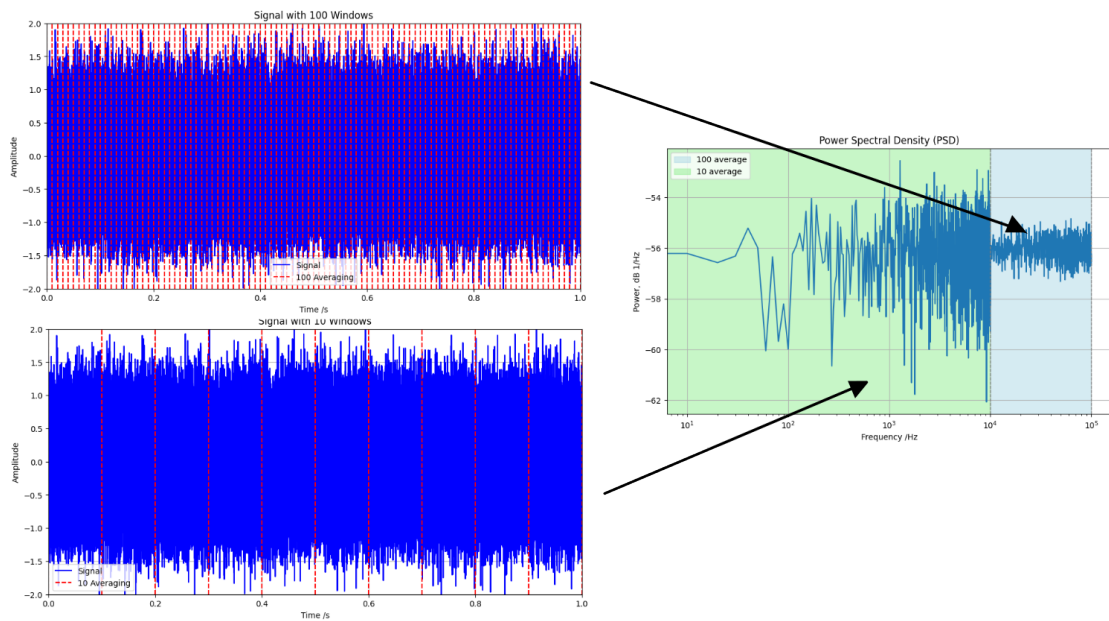


Figure A.1: Two possibility of window framing are showed bigger windows used for lower Fourier bins, smaller one for higher Fourier bins

Starting from the idea of a variable windowing system two new algorithms of PDS or CSD are possible:

- **Maximum average** The number of averages decreases for every decades starting from the higher decades with the maximum averaging-factor going downwards to the last decade where the averaging-factor is 1.
- **Minimum-Maximum average** The number of averages has a minimum and maximum point starting from the lower decades with smaller averaging-factors going upwards to higher decades with bigger averaging-factors.

A.3.1 Python Code with Maximum Averages

```
Csd_MA

def Csd_MA(x, y, fs, Max_avg, N, win_type):

    #Power Spectral Density Bertlett with Maximum Average
    CSD = []
    fr = []
    j=0
```

```

averages=[]
decades=[]

while(True):

    Window=int(N/(Max_avg/(10**j)))
    win = signal.windows.get_window(win_type,Window)

    buff = []
    buff2 = []
    csd_cross= []

    averages.append((Max_avg/(10**j)))

    for i in range(int(Max_avg/(10**j))):

        X = fourier.fft(x[i*Window:i*Window+Window]*
win)
        Y = fourier.fft(y[i*Window:i*Window+Window]*
win)

        app= 2*(1/fs)*Y*np.conj(X)/((win*win).sum())
        csd_cross.append(app)

    buff = np.array(csd_cross)
    buff2 = (np.sum(buff , axis=0)/(Max_avg/(10**j)))
    freq =[]

    freq = np.linspace(0,fs,int(len(x)/(Max_avg/(10**
j))))

    f_min = (fs/2)/(10**(j+1))
    f_max = (fs/2)/(10**(j))

    decades.append(f_max)

    j=j+1

    if Window == N:

        f_min = 0
        mask = (freq >= f_min) & (freq <= f_max)

        CSD.extend(buff2[mask])
        fr.extend(freq[mask])

        #append the last frequency value when the
maximum is reached

```

```

        decades.append(0)

        #final index sorting
        sorted_indices = np.argsort(fr)
        fr = np.array(fr)[sorted_indices]
        CSD = np.array(CSD)[sorted_indices]

        return fr[0:int(N/2)], np.array(CSD[0:int(N
/2)]), np.array(averages), np.array(decades)

    mask = (freq >= f_min) & (freq <= f_max)

    CSD.extend(buff2[mask])
    fr.extend(freq[mask])

    #final index sorting
    sorted_indices = np.argsort(fr)
    fr = np.array(fr)[sorted_indices]
    CSD = np.array(CSD)[sorted_indices]

    return fr[0:int(N/2)], np.array(CSD[0:int(N/2)]), np.
array(averages), np.array(decades)

```

A.3.2 Python Code with Minimum-Maximum Averages

Csd_Min_Max

```

def Csd_Min_Max(x, y, fs, Min_avg, Max_avg, N, win_type):

    CSD = []
    fr = []
    j=0
    averages=[]
    decades=[]

    while(True):

        Window=int(len(x)/(Max_avg/(10**j)))
        win = signal.windows.get_window(win_type,Window)

        buff = []
        buff2 = []
        csd_cross= []

```

```

averages.append((Max_avg/(10**j)))

for i in range(int(Max_avg/(10**j))):

    X = fourier.fft(x[i*Window:i*Window+Window]*win)
    Y = fourier.fft(y[i*Window:i*Window+Window]*win)
    app= 2*(1/fs)*Y*np.conj(X)/((win*win).sum())
    csd_cross.append(app)

buff = np.array(csd_cross)
buff2 = (np.sum(buff , axis=0)/(Max_avg/(10**j)))
freq = []

freq = np.linspace(0,fs,int(len(x)/(Max_avg/(10**j))))
)

f_min = (fs/2)/(10**(j+1))
f_max = (fs/2)/(10**(j))

decades.append(f_max)

j=j+1

if Window == int(len(x)/(Min_avg)):

    f_min = 0
    mask = (freq >= f_min) & (freq <= f_max)

    CSD.extend(buff2[mask])
    fr.extend(freq[mask])

    #append the last frequency value when the maximum
is reached
    decades.append(0)

    #final index sorting
    sorted_indices = np.argsort(fr)
    fr = np.array(fr)[sorted_indices]
    CSD = np.array(CSD)[sorted_indices]

    return fr[0:int(N/2)], np.array(CSD[0:int(N/2)]),
np.array(averages), np.array(decades)

mask = (freq >= f_min) & (freq <= f_max)

CSD.extend(buff2[mask])

```

```
fr.extend(freq[mask])

#final index sorting
sorted_indices = np.argsort(fr)
fr = np.array(fr)[sorted_indices]
CSD = np.array(CSD)[sorted_indices]

return fr[0:int(N/2)], np.array(CSD[0:int(N/2)]), np.
array(averages), np.array(decades)
```

Appendix B

Example of Cross-correlation Estimation

Code referred to the example presented in the chapter section that analyse the impact of the optimum cross-spectrum estimator. This code is functional to prove some observation about the imprudent usage of the magnitude of the cross-spectrum as cross-correlation estimator [30].

estimation example

```
from Spectra_lib import Spectra
import numpy as np
import matplotlib.pyplot as plt
spec = Spectra()

plt.figure(1)

# Number of samples
num_samples = 20000000

# white noise with a normal distribution
a = np.random.normal(loc=0.0, scale=0.04, size=num_samples)
b = np.random.normal(loc=0.0, scale=0.04, size=num_samples)
c = np.random.normal(loc=0.0, scale=0.02, size=num_samples)

#flicker noise
d = np.random.normal(0, 2, num_samples)
d = np.cumsum(d)
```

```

d = d / np.std(d)

f, fft, avgerages, decades =
spec.Csd_MA(d,d,200000,10000,num_samples/10)
plt.semilogx(f,10*np.log10(abs(fft)),label = r'$S_d$')

f, fft, avgerages, decades =
spec.Csd_MA(c,c,200000,10000,num_samples/10)
plt.semilogx(f,10*np.log10(abs(fft)),label = r'$S_c$')

f, fft, avgerages, decades =
spec.Csd_MA(b,b,200000,10000,num_samples/10)
plt.semilogx(f,10*np.log10(abs(fft)),label = r'$S_a$')

f, fft, avgerages, decades =
spec.Csd_MA(a,a,200000,10000,num_samples/10)
plt.semilogx(f,10*np.log10(abs(fft)),label = r'$S_b$')

spec.marker_plotter_MA(avgerages, decades)
plt.xlim(1,max(decades))

plt.xlabel('Frequency [Hz]')
plt.ylabel('PSD [dB]')
plt.legend()
plt.grid()
plt.show()

plt.figure(2)

f, fft, avgerages, decades =
spec.Csd_MA(a+c+d,b+c+d,200000,10000,num_samples/10)
plt.semilogx(f,10*np.log10(abs(fft)),label = r'$S_{x,y}$')

f, fft, avgerages, decades =
spec.Csd_MA(a+c+d,b+c-d,200000,10000,num_samples/10)

plt.semilogx(f,10*np.log10(np.real(fft)),label =
r'$Re\{S_{x,\tilde{y}}\}$ (real part positive)',
color='orange')

plt.semilogx(f,10*np.log10(-np.real(fft)),label =
r'$-Re\{S_{x,\tilde{y}}\}$ (real part negative)',

```

```
color='red')

spec.marker_plotter_MA(avverages, decades)

plt.xlim(1,max(decades))
plt.xlabel('Frequency [Hz]')
plt.ylabel('CSD [dB]')
plt.legend(fontsize = 15)
plt.grid()
plt.show()
```

Appendix C

Allan Variance

Allan variance, also known as two-sample variance, is a statistical tool used to evaluate the stability of frequency signals over time. Traditional variance measures, such as standard deviation, are not well suited for analyzing time-dependent fluctuations in frequency signals, as they tend to diverge for many types of noise processes commonly found in oscillators and clocks. In contrast, Allan variance is specifically designed to capture both short-term and long-term variation [42].

Definition

The Allan *VAR*iance (AVAR) is defined as the mean square value of the differences of M contiguous couple of samples acquired at the frequency $1/\tau$. Mathematically, it is expressed as:

$$\sigma_y^2(\tau) = \frac{1}{2(M-1)} \sum_{k=1}^{M-1} (x_{i+1} - x_i)^2 \quad (\text{C.1})$$

The Allan *DEV*iation (ADEV) is the square root of Allan variance.

$$\sigma_y(\tau) \quad (\text{C.2})$$

A typical clock signal can be represented as:

$$v(t) = V_0[1 + \alpha]\cos(2\pi\nu_0 t + \phi(t)) \quad (\text{C.3})$$

where :

- V_0 is the nominal amplitude of the signal,
- α represents small amplitude fluctuations,
- ν_0 is the nominal frequency,

- $\phi(t)$ is the phase noise, which encapsulates the instability in the phase of the signal.

In high-precision applications, phase noise $\phi(t)$ plays a crucial role in determining the overall performance of the frequency source. The frequency deviation from the nominal frequency $y(t)$ is obtained by differentiating this phase fluctuations:

$$y(t) = \frac{1}{2\pi\nu_0} \frac{d\phi(t)}{dt} \tag{C.4}$$

An alternative representation of the Allan variance can be derived by the frequency error signal. It is expressed as an integral over the power spectral density $S_y(f)$, which characterizes the distribution of frequency fluctuations over different frequency components [43]:

$$\sigma_y^2(\tau) = \int_0^\infty S_y(f) \frac{\sin^4(2f\tau)}{(2f\tau)^2} df \tag{C.5}$$

This equation provides a bridge between time-domain and frequency-domain analysis, allowing researchers to infer the types of noise present in the system by examining the behavior of $S_y(f)$. Different types of noise, such as white frequency noise, flicker frequency noise, and random walk frequency noise, exhibit distinct dependencies on τ , which makes Allan variance a powerful diagnostic tool.

Appendix D

Fitting Models

The python library "curve_fit" is used in order to plot absorption curves of rubidium. The code snippet below introduces the definition of the used functions.

```
from scipy.optimize import curve_fit
from scipy.special import voigt_profile
```

The functions that approximate the measured plots are a combination of functions like explained in the theoretical chapters. The approximated behavior is extracted by the following representation only to extract the linear modulation caused by power increment or decrement.

```
def lorentzian_plus_rect(x, slope, intercept, A, x0, gamma):
    y = slope*x + intercept -
    A* ((gamma/2)**2) / ((x - x0)**2 + ((gamma/2)**2))
    return y

def lorentzian(x, A, x0, gamma):
    y = 1
    - A* ((gamma/2)**2)/((x - x0)**2 + ((gamma/2)**2))
    return y

def gaussian_plus_rect(x, slope, intercept, A, x0, sigma):
    y = slope*x + intercept
    - A*np.exp(-(x-x0)**2/(2*sigma**2))
    return y
```

```
def gaussian(x,A,x0,sigma):
    y = 1 - A*np.exp(-(x-x0)**2/(2*sigma**2))
    return y
```

After the linear compensation offered by upper functions the function is fitted by a more accurate model, an example of Vogit and Gaussian models is offered in the blue box below.

```
def triple_gaussian(x, slope, intercept, A, x0, sigma):

    C_F1 = A/18
    C_F2 = (5*A)/18
    C_F3 = (7*A)/9

    y = - C_F1/sigma*np.exp(-(x-x0)**2/(2*sigma**2))
    - C_F2/sigma*np.exp(-(x-x0-0.15695)**2/(2*sigma**2))
    - C_F3/sigma*np.exp(-(x-x0-0.4236)**2/(2*sigma**2))

    return y
```

The usage of the fitting function is the following:

```
# initial parameters
initial_guess =
[-0.04,0.9,0.2,-0.5,2.5]

# function interrogation
params, covariance =
curve_fit(lorentzian_plus_rect, x, y, p0 = initial_guess)

# parameter extraction
slope, intercept, A, x0, gamma =
parameters
```

Like seen up-above three step are performed in a recursive usage method. The user inserts an initial parameter attempt, the `curve_fit` function perform a fit and after

that parameter are extracted and the user can plot them and compare the fitted and the real function. If the two functions don't overlap perfectly the parameter mus be changed a bit to allow the convergence of the method.

Bibliography

- [1] William J Riley. «A history of the rubidium frequency standard». In: *IEEE UFFC-S History* (2019), p. 2. URL: <https://www.wriley.com/A%20History%20of%20the%20Rubidium%20Frequency%20Standard.pdf> (cit. on pp. 1, 3, 8).
- [2] Godone A. Micalizio S. Calosso C.E. and Levi F. «Metrological characterization of the pulsed Rb clock with optical detection». In: *Metrologia* 49.4 (2012), pp. 425–432. DOI: 10.1088/0026-1394/49/4/425 (cit. on pp. 1, 5).
- [3] James Camparo. «The Rubidium Atomic Clock and Basic Research». In: *Physics Today - PHYS TODAY* 60 (Dec. 2007), p. 12. DOI: 10.1063/1.2812121 (cit. on p. 1).
- [4] Michael Lombardi. «The evolution of time measurement, part 3: Atomic clocks [Recalibration]». In: *IEEE Instrum. Meas. Mag.* 14 (Dec. 2011), pp. 46–49. DOI: 10.1109/MIM.2011.6086901 (cit. on p. 3).
- [5] *A Brief History of Atomic Time*. URL: <https://www.nist.gov/atomic-clocks/brief-history-atomic-time> (cit. on p. 3).
- [6] Mohammed Ziaur Rahman. «Beyond trilateration: GPS positioning geometry and analytical accuracy». In: *Global Navigation Satellite Systems: Signal, Theory and Applications* (2012), pp. 241–256 (cit. on p. 4).
- [7] Bernardo Jaduszliwer and James Camparo. «Past, present and future of atomic clocks for GNSS». In: *GPS Solutions* 25 (2021), pp. 1–13. DOI: 10.1007/s10291-020-01059-x (cit. on p. 4).
- [8] URL: <https://safran-navigation-timing.com/wp-content/uploads/2023/03/RAFS-SAFRAN-Datasheet.pdf> (cit. on p. 4).
- [9] Gabriela D Martinez, Chao Li, Alexander Staron, John Kitching, Chandra Raman, and William R McGehee. «A chip-scale atomic beam clock». In: *Nature Communications* 14.1 (2023), p. 3501. DOI: 10.1038/s41467-023-39166-1 (cit. on p. 5).

- [10] John Kitching. *Chip-Scale Clocks*. 2020. URL: <https://www.nist.gov/noac/technology/time-and-frequency/chip-scale-clocks#:~:text=In%202004%2C%20NIST%20scientists%20created%20the%20first%20chip-scale%2C%20researchers%20have%20focused%20on%20improvements%20to%20its%20design>. (cit. on p. 5).
- [11] Norman F Ramsey. «A new molecular beam resonance method». In: *Physical Review* 76.7 (1949), p. 996. DOI: 10.1103/PhysRev.76.996 (cit. on p. 6).
- [12] M Arditi and TR Carver. «Atomic clock using microwave pulse-coherent techniques». In: *IEEE Transactions on Instrumentation and Measurement* 2/3 (1964), pp. 146–152. DOI: 10.1109/TIM.1964.4313389 (cit. on p. 7).
- [13] Christopher J Foot. *Atomic physics*. Vol. 7. Oxford university press, 2005 (cit. on pp. 7, 53, 55).
- [14] S. Micalizio, F. Levi, C.E. Calosso, M. Gozzelino, and A. Godone. «A pulsed-laser Rb atomic frequency standard for GNSS applications». In: *GPS Solutions* 25.3 (2021), p. 94. DOI: 10.1007/s10291-021-01136-9 (cit. on p. 8).
- [15] A Godone, Filippo Levi, CE Calosso, and Salvatore Micalizio. «High-performing vapor-cell frequency standards». In: *La Rivista del Nuovo Cimento* 38 (2015), pp. 133–171. DOI: 10.1393/ncr/i2015-10110-4 (cit. on p. 8).
- [16] RH Dicke. «The effect of collisions upon the Doppler width of spectral lines». In: *Physical Review* 89.2 (1953), p. 472. DOI: 10.1103/physrev.89.472 (cit. on p. 8).
- [17] M Arditi and TR Carver. «Frequency shift of the zero-field hyperfine splitting of Cs 133 produced by various buffer gases». In: *Physical Review* 112.2 (1958), p. 449. DOI: 10.1103/PhysRev.112.449 (cit. on p. 8).
- [18] Claudio Eligio Calosso, Michele Gozzelino, Aldo Godone, Haixiao Lin, Filippo Levi, and Salvatore Micalizio. «Intensity detection noise in pulsed vapor-cell frequency standards». In: *IEEE Transactions on Ultrasonics, Ferroelectrics, and Frequency Control* 67.5 (2019), pp. 1074–1079. DOI: 10.1109/TUFFC.2019.2957418 (cit. on p. 9).
- [19] Fritz Riehle. *Frequency standards: basics and applications*. John Wiley & Sons, 2006 (cit. on pp. 9, 10).
- [20] Filippo Levi, CE Calosso, A Godone, and S Micalizio. «Pulsed optically pumped Rb clock: a high stability vapor cell frequency standard». In: *2013 Joint European Frequency and Time Forum & International Frequency Control Symposium (EFTF/IFC)*. IEEE. 2013, pp. 599–605 (cit. on p. 11).
- [21] Klaus Petermann. *Laser diode modulation and noise*. Vol. 3. Springer Science & Business Media, 1991 (cit. on p. 13).

- [22] Rob J Fronen and Lode KJ Vandamme. «Low-frequency intensity noise in semiconductor lasers». In: *IEEE Journal of quantum electronics* 24.5 (1988), pp. 724–736. DOI: 10.1109/3.188 (cit. on p. 13).
- [23] Kenichiro Aoki and Takahisa Mitsui. «Observing random walks of atoms in buffer gas through resonant light absorption». In: *Physical Review A* 94.1 (2016), p. 012703. DOI: 10.1103/PhysRevA.94.012703 (cit. on pp. 15, 16).
- [24] S Micalizio, A Godone, M Gozzelino, and F Levi. «Brownian motion-induced amplitude noise in vapor-cell frequency standards». In: *New Journal of Physics* 22.8 (2020), p. 083050 (cit. on p. 16).
- [25] JC Camparo and JG Coffey. «Conversion of laser phase noise to amplitude noise in a resonant atomic vapor: The role of laser linewidth». In: *Physical Review A* 59.1 (1999), p. 728. DOI: 10.1103/PhysRevA.59.728 (cit. on p. 17).
- [26] Enrico Rubiola, Kirill Volyanskiy, and Laurent Larger. «Measurement of the laser relative intensity noise». In: *2009 IEEE International Frequency Control Symposium Joint with the 22nd European Frequency and Time Forum (EFTF)*. IEEE, 2009, pp. 50–53. DOI: 10.1109/FREQ.2009.5168140 (cit. on pp. 20, 28).
- [27] Enrico Rubiola. «The magic of cross correlation in measurements from DC to optics». In: *Proceedings of the 22nd European Frequency and Time Forum (EFTF)*. 2008. URL: <https://rubiola.org/pdf-articles/conference/2008-eftf-magic-correlation.pdf> (cit. on p. 21).
- [28] Enrico Rubiola and François Vernotte. «The cross-spectrum experimental method». In: *arXiv preprint arXiv:1003.0113* (2010). DOI: 10.48550/arXiv.1003.0113 (cit. on p. 25).
- [29] Yannick Gruson, Adrian Rus, Ulrich L Rohde, Alexander Roth, and Enrico Rubiola. «Artifacts and errors in cross-spectrum phase noise measurements». In: *Metrologia* 57.5 (2020), p. 055010. DOI: 10.1088/1681-7575/ab8d7b (cit. on p. 26).
- [30] Craig W Nelson, Archita Hati, and David A Howe. «Phase inversion and collapse of cross-spectral function». In: *Electronics letters* 49.25 (2013), pp. 1640–1641. DOI: 10.1049/e1.2013.3022 (cit. on pp. 27, 82).
- [31] T. Mitsui and K. Aoki. «Noise reduction and hyperfine level coherence in spontaneous noise spectroscopy of atomic vapor». In: *JOSA B* 31.2 (2014), pp. 195–200. DOI: 10.1364/JOSAB.31.000195 (cit. on p. 29).
- [32] *Keysight DAQ970A*. URL: <https://www.keysight.com/us/en/assets/7018-06259/technical-overviews/5992-3168.pdf> (cit. on p. 32).

- [33] *single photodiode Thorlabs PDA36A2 datasheet*. URL: <https://www.thorlabs.com/drawings/842c0c322893a6e-6039A12F-B332-342C-5E11735F0A763861/PDA36A2-Manual.pdf> (cit. on p. 39).
- [34] *balanced photodiode Thorlabs PDB250A datasheet*. URL: <https://www.thorlabs.de/drawings/9c27470b363b2ccd-60287654-B39A-0171-C99B81FAAC235F1D/PDB250A-Manual.pdf> (cit. on p. 42).
- [35] Shruti Jose Maliakal. «Experiments on saturated absorption in atomic vapour». PhD thesis. IISERM, 2019. URL: <http://hdl.handle.net/123456789/1139> (cit. on p. 58).
- [36] Paul Siddons, Charles S Adams, Chang Ge, and Ifan G Hughes. «Absolute absorption on rubidium D lines: comparison between theory and experiment». In: *Journal of Physics B: Atomic, Molecular and Optical Physics* 41.15 (2008), p. 155004. DOI: 10.1088/0953-4075/41/15/155004 (cit. on p. 58).
- [37] Matthew D Rotondaro and Glen P Perram. «Collisional broadening and shift of the rubidium D1 and D2 lines (52S12→ 52P12, 52P32) by rare gases, H2, D2, N2, CH4 and CF4». In: *Journal of Quantitative Spectroscopy and Radiative Transfer* 57.4 (1997), pp. 497–507. DOI: 10.1016/S0022-4073(96)00147-1Getrightsandcontent (cit. on p. 60).
- [38] Milton Abramowitz and Irene A Stegun. *Handbook of mathematical functions with formulas, graphs, and mathematical tables*. Vol. 55. US Government printing office, 1968. DOI: 10.2307/2004114 (cit. on p. 60).
- [39] Modestino Carbone, Giovanni Costanzo, Claudio Calosso, Michele Gozzelino, Filippo Levi, and Salvatore Micalizio. «PM/Am Conversion Measurement for Narrow-Linewidth Lasers with Rin and Shot-Noise Reduction». In: *Poster of the 38th European Frequency and Time Forum (EFTF)* (2025) (cit. on p. 68).
- [40] Modestino Carbone. *Spectra_{ib}.py*. 2025. URL: https://github.com/modestinocarbone/Spectra_lib (cit. on p. 69).
- [41] Gerhard Heinzl, Albrecht Rüdiger, and Roland Schilling. «Spectrum and spectral density estimation by the Discrete Fourier transform (DFT), including a comprehensive list of window functions and some new at-top windows». In: (2002). URL: https://pure.mpg.de/rest/items/item_152164/component/file_152163/content (cit. on p. 73).
- [42] Enrico Rubiola and Francois Vernotte. «The companion of Enrico’s chart for phase noise and two-sample variances». In: *IEEE Transactions on Microwave Theory and Techniques* 71.7 (2023), pp. 2996–3025 (cit. on p. 85).

- [43] DW Allan. *Conversion of Frequency Stability Measures from the Time-domain to the Frequency-domain, vice-versa and Power-law Spectral Densities*. 2012. URL: http://www.allanstime.com/Publications/DWA/Conversion_from_Allan_variance_to_Spectral_Densities.pdf (cit. on p. 86).